

Article

# Multi-Objective Topology Optimization of the Cooling Plate for Battery Thermal Management

Tianshuo Yang <sup>1,2</sup> , Huaqiang Liu <sup>1,\*</sup> , Wenjie Zhang <sup>1</sup>, Aoshuang Ding <sup>3</sup> and Mengke Wu <sup>4</sup>

<sup>1</sup> Naval Architecture and Ocean Engineering College, Dalian Maritime University, Dalian 116026, China; yts3440926281@dltmu.edu.cn (T.Y.); zhangwenjie@dltmu.edu.cn (W.Z.)

<sup>2</sup> Houston International Institute, Dalian Maritime University, Dalian 116026, China

<sup>3</sup> CSSC Jiujiang Boiler Co., Ltd., Jiujiang 332000, China

<sup>4</sup> Locomotive Development Department, CRRC Dalian Locomotive and Rolling Stock Co., Ltd., Dalian 116022, China

\* Correspondence: huaqiang.liu@dltmu.edu.cn

## Abstract

The lifespan and performance of power batteries used in electric vehicles and ships are highly sensitive to the operating temperatures, demonstrating the indispensable role of an effective thermal management system. Topology optimization is a method that can achieve comprehensive optimization of thermal and flow performance. The inlet/outlet layout is an important parameter affecting the thermal management performance of topology-optimized channels. To optimize the inlet/outlet positions, this study establishes the relationship between inlet/outlet positions and evaluation indicators using the response surface method, and further obtains the optimal solution based on the NSGA II and TOPSIS algorithms. The results show that the topology-optimized liquid cooling plate with optimal inlet/outlet position (TOPO) presents a lower maximum temperature under different inlet velocities than the counterparts with the conventional inlet/outlet layout (0.13–0.22 K), straight channel with the optimal inlet/outlet position (0.89–1.03 K), and single inlet/outlet straight channel (1.8–2.6 K). Moreover, the comprehensive performance of the proposed TOPO is more pronounced at high inlet velocity conditions. When the inlet velocity is 0.13 m/s, compared with the other counterparts, the performance evaluation criterion of TOPO increases by 16.6%, 28.7%, and 79.4%, respectively.



Academic Editors: Johan E. ten Elshof and Yong-Joon Park

Received: 20 August 2025

Revised: 10 October 2025

Accepted: 31 October 2025

Published: 4 November 2025

**Citation:** Yang, T.; Liu, H.; Zhang, W.; Ding, A.; Wu, M. Multi-Objective Topology Optimization of the Cooling Plate for Battery Thermal Management. *Batteries* **2025**, *11*, 406. <https://doi.org/10.3390/batteries11110406>

**Copyright:** © 2025 by the authors. Licensee MDPI, Basel, Switzerland. This article is an open access article distributed under the terms and conditions of the Creative Commons Attribution (CC BY) license (<https://creativecommons.org/licenses/by/4.0/>).

## 1. Introduction

In recent years, more and more environmental problems have gradually emerged and gained attention [1]. Among them, as the number of traditional gasoline-powered vehicles continues to increase and as they are still being widely used, the problems of greenhouse gas emissions and the energy crisis have become increasingly serious [2]. Against this backdrop, promoting more environmentally friendly electric vehicles is regarded as the core solution [3]. Because of their high stability, low self-discharge rate, and high energy density, lithium-ion batteries are widely used as the power source for electric vehicles [4]. However, the safety and electrochemical performance of lithium-ion batteries are extremely sensitive to their operating temperature [5]. Studies have shown that the suitable operating temperature range for lithium-ion batteries is 15–35 °C, and the maximum temperature difference inside the battery cannot exceed 5 °C [6]. During operation, the internal resistance

and chemical reactions of the battery will continuously generate heat, which makes it impossible to control the temperature within the suitable range. This will damage the battery's lifespan and capacity. In severe cases, it may even lead to thermal runaway, resulting in fires, explosions, and other disasters [7]. Therefore, it is necessary to take appropriate intervention measures to prevent these dangers.

According to the cooling medium, battery thermal management systems (BTMSs) can be roughly classified into air cooling, liquid cooling, phase change material (PCM) cooling, and hybrid cooling [8]. The air-cooled BTMS achieves cooling by transferring the battery's heat to the air, and it has advantages such as low cost, simple structure, and no risk of leakage [9]. However, its poor heat transfer efficiency cannot meet the cooling requirements of batteries under high-rate discharge [10]. The BTMS based on PCM utilizes solid–liquid phase change to absorb heat and is considered a promising approach. However, the thermal conductivity of commonly used phase change materials is relatively low, and their cooling capacity is very limited after multiple charge–discharge cycles [11]. Meanwhile, due to the limitation of its phase change temperature range, it is difficult to be widely implemented in practical applications [12]. Liquid BTMS has been widely used by the electric vehicle market due to its high heat transfer coefficient and moderate manufacturing and maintenance costs [13]. In addition, the feasibility of hybrid BTMS designs, which could combine the advantages of different cooling methods [14,15], has been actively explored in recent years, such as liquid–PCM coupled BTMSs and liquid–heat pipe coupled BTMSs [16]. However, hybrid BTMSs are still under development and their feasibility remains to be proven [17]. Therefore, the BTMSs based on liquid coolants are still the prevalent option for practical application, especially in electric vehicles and ships.

The key to the performance of the liquid battery thermal management system lies in the channel structure of the liquid cooling plate [18]. In recent years, researchers have made many attempts to perfect the design of the channel structure of the liquid cooling plate. The most common channel structures are straight channels and serpentine channels. Many researchers have explored this. Liu et al. [19] introduced cross channels into the traditional serpentine channels and found that the V-shaped cross channels had the optimal structural parameters, achieving the best thermal performance: the number of crossings was seven, the width was 2.0 mm, and the angle was 45°. In addition, researchers were inspired by biological structures and proposed various biomimetic channel flow structure designs. Fan et al. [20], inspired by biomimetics, proposed a novel double-layer tree-shaped channel, and found that compared with the serpentine flow channel, its maximum temperature and standard deviation of surface temperature were reduced by 1.79% and 69.25%, respectively, and the pressure drop was reduced by 79.13%. Moreover, based on the traditional channel structure and biomimetic channel structure, researchers used optimization algorithms to optimize key parameters to improve performance. Xia et al. [21], based on the leaf vein biomimetic flow channel, used the NSGA-II algorithm to optimize four structural parameters: the distance from the outlet to the hexagon, the distance from the inlet to the hexagon, the spacing between adjacent hexagons, and the size of the hexagon. The results showed that the optimized liquid cooling plate had a pressure drop reduced by 14.2%, and a maximum temperature reduced by 0.7 °C. However, the structures of these liquid cooling plates are all proposed based on the researchers' experience. The optimization of structural parameters is also based on the fixed structures already proposed. This leads to very limited performance improvement brought on by the optimization.

The topology optimization method transforms the problem of optimizing the battery thermal management performance into a mathematical problem based on the actual geometric model and application scenarios. This approach significantly enhances the innovation and design freedom of the liquid cooling plate structure design, and frees the design

from the limitations of researchers' experience and ideas. In addition, multi-objective topology optimization enables the liquid cooling plate structure to achieve a balance between thermal performance and flow performance. With the development of additive manufacturing technology, the cost of manufacturing complex geometric components such as topology-optimized liquid cooling plates has been significantly reduced [22]. Therefore, the application of the topology optimization method to design liquid cooling plate structures is becoming increasingly widespread. Zhan et al. [23] explored the effects of inlet and outlet arrangement direction, quantity, channel depth, and total inlet mass flow rate on the performance of the liquid cooling plate. The results indicated that when adopting three inlets and three outlets in the width direction, with a channel depth of 3 mm and an inlet total mass flow rate of 15 g/s, the system heat dissipation and power consumption could achieve the best balance. Wang et al. [24] obtained two liquid cooling plate structures based on laminar and turbulent topology optimization. The results showed that the liquid cooling plate obtained through topology optimization under turbulent conditions achieved the best overall cooling effect. Zhan et al. [25] discussed the inlet and outlet positions of a single inlet and single outlet, and found that the parallel diagonal structure could minimize the pressure drop to the greatest extent, while the straight-in and straight-out structure performed best in terms of the highest temperature and temperature deviation. Lin et al. [26] established the relationship between Reynolds number, target function weight coefficients, and cooling performance through the response surface method (RSM), and further obtained the optimal design parameters using the NSGA-II algorithm.

Based on the above literature review, Zhan et al. [23] pointed out that the liquid cooling plate with three inlets and three outlets in the width direction has superior performance. However, at present, there is a lack of research on the optimal inlet and outlet locations for this situation. Wu et al. [27] adopted the layout where the two side inlets and outlets were placed at the outermost edges for the three-inlet and three-outlet configuration. Zhan et al. [25] discussed and analyzed representative examples of inlet and outlet positions with a single inlet and a single outlet. The results showed that there was a representative example for each in terms of thermal performance and flow performance. This method of listing and analyzing some of the inlet and outlet positions was not comprehensive and had difficulties identifying the optimal inlet and outlet positions that achieved the best overall thermal and flow performance. Lin et al. [26] established the relationship between design variables and the target function using the response surface method, providing a new approach. Based on the research gaps and current research status, the main work of this paper is as follows: 1. Based on the layout of three inlets and three outlets in the width direction, establish the relationship between the inlet/outlet position parameters and the key evaluation indicators of BTMS. 2. Use the NSGA-II algorithm to obtain the Pareto front and use TOPSIS to obtain the optimal solution for the inlet/outlet position parameters. 3. Conduct a comprehensive performance comparison between the topology-optimized liquid cooling plate with the optimal inlet/outlet positions, the topology-optimized liquid cooling plate with conventional inlet/outlet positions, and the straight channel. Furthermore, investigate the influence of inlet flow velocity on the observed performance differences.

## 2. Two-Dimensional Topology Optimization Design

Figure 1 presents the topology optimization concept design model of conjugate heat transfer applied to the thermal management system of liquid batteries. The design region is regarded as a porous medium, and the solid area and fluid area are distinguished by introducing design variables  $\gamma$ . The design variables vary continuously from 0 to 1, where  $\gamma = 1$  corresponds to the fluid region, and  $\gamma = 0$  corresponds to the solid region.

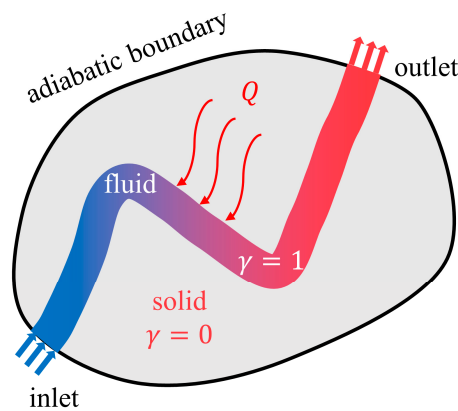


**Figure 1.** The conceptual model of topology optimization design.

## 2.1. Mathematical Model of Topology Optimization

### 2.1.1. Flow Equations

Assume that the fluid is incompressible, and the flow state within the channel is laminar, with the Reynolds number being less than 2300. Therefore, the continuity equation and the momentum equation can be expressed as follows:

$$\nabla \cdot u = 0 \quad (1)$$

$$\rho(u \cdot \nabla)u = -\nabla P + \mu\nabla^2u + F \quad (2)$$

where  $\rho$  represents the density of the fluid,  $u$  represents the velocity of the fluid,  $P$  represents the pressure,  $\mu$  represents the viscosity, and  $F$  represents the flow resistance. Under the assumption of porous media [28], the size of  $F$  is proportional to the speed of the fluid flow, which can be expressed as follows:

$$F = -\alpha u \quad (3)$$

where  $\alpha$  represents the inverse permeability of the porous medium.

The inverse permeability is interpolated based on the design variables  $\gamma$  using the Darcy interpolation function, which is expressed as follows:

$$\alpha(\gamma) = \alpha_s + (\alpha_s - \alpha_f) \frac{q(1 - \gamma)}{q + \gamma} \quad (4)$$

where  $q$  is the penalty factor, with a value of 0.01 in this paper.  $\alpha_f$  is the inverse permeability of the fluid, which should be a very small value ( $\approx 0$ ).  $\alpha_s$  is the inverse permeability of the solid, which is a function of the Reynolds number  $Re$  and the Darcy number  $Da$ , expressed as follows:

$$\alpha_s = \left(1 + \frac{1}{Re}\right) \frac{1}{Da} \quad (5)$$

### 2.1.2. Heat Transfer Equations

Assume that the heat transfer process is stable and the physical properties of each material do not change with temperature. During the heat transfer process, the heat transfer modes in the fluid domain and the solid domain are different. The corresponding equations are as follows:

$$\rho C_p(u \cdot \nabla)T = k_f \nabla^2 T \text{ (in fluid)} \quad (6)$$

$$0 = k_s \nabla^2 T + Q \text{ (in solid)} \quad (7)$$

where  $C_p$  is the specific heat capacity of the fluid,  $k_f$  is the thermal conductivity of the fluid,  $k_s$  is the thermal conductivity of the solid, and  $Q$  is the heat generation in the solid region.

By combining Equations (6) and (7) and introducing design variables  $\gamma$ , the following equation is obtained:

$$\gamma \rho C_p (u \cdot \nabla) T = [(1 - \gamma) k_s + \gamma k_f] \nabla^2 T + (1 - \gamma) Q \quad (8)$$

where the heat source  $Q$  is proportional to the temperature difference, which can be expressed as follows:

$$Q = h(T_Q - T) \quad (9)$$

where  $T_Q$  represents the reference temperature of the ideal heat source.

### 2.1.3. Dimensionless Processes

In order to save computing resources and improve the convergence of the calculation, the governing equations are subjected to dimensionless processing. The dimensionless gradient operator  $\nabla^*$ , the dimensionless velocity  $u^*$ , the dimensionless pressure  $p^*$ , the dimensionless temperature  $T^*$ , the dimensionless heat generation coefficient  $h^*$ , the fluid's constant-pressure specific heat capacity  $C_p$ , and the Reynolds number  $Re$  are defined as follows:

$$\begin{aligned} \nabla^* &= L \nabla, u^* = \frac{u}{U}, p^* = \frac{p - p_0}{\rho U^2}, Re = \frac{\rho U L}{\mu} \\ T^* &= \frac{T - T_{in}}{T_r - T_{in}}, h^* = \frac{h L^2}{k_f}, C_p = Re \cdot Pr \end{aligned} \quad (10)$$

where  $L$  represents the characteristic length,  $U$  is the characteristic velocity,  $p_0$  is the reference pressure,  $T_{in}$  is the inlet temperature,  $h^*$  is the dimensionless heat generation coefficient,  $Pr$  is the Prandtl number, and  $T_r$  is the reference temperature. The value of temperature  $T_r$  referred to in this article is the equivalent temperature  $T_Q$  of an ideal heat source. After performing dimensionless processing on the expressions Equations (1), (2), and (8), the following expressions can be obtained:

$$\nabla^* \cdot u^* = 0 \quad (11)$$

$$\rho(u^* \cdot \nabla^*) u^* = -\nabla^* p^* + \frac{1}{Re} \nabla^{*2} u^* - \left(1 + \frac{1}{Re}\right) \frac{1}{Da} \frac{q(1 - \gamma)}{q + \gamma} u^* \quad (12)$$

$$\gamma Re Pr (u^* \cdot \nabla^*) T^* = [(1 - \gamma) K + \gamma] \nabla^* T^* + (1 - \gamma) h^* (1 - T^*) \quad (13)$$

### 2.2. Density Filter and Projection

The optimization results are prone to be affected by the grid-related factors, and usually exhibit a checkerboard pattern, thereby reducing the stability and reliability of the optimization process. To address this issue, in the entire optimization process of this study, the Helmholtz density filter [29] was employed:

$$-r_f^2 \nabla^2 \gamma_n + \gamma_n = \gamma \quad (14)$$

where  $r_f$  is the filter radius and  $\gamma_n$  is the new design variable obtained after filtering.

The Helmholtz density filtering method often causes the boundaries between fluids and solids to become blurred, making it difficult to clearly define the boundaries for practical applications. In order to further reduce the gray area and make the fluid–solid boundary clearer, the hyperbolic tangent projection [30] is used throughout the entire topology optimization process:

$$\gamma_p = \frac{\tanh(\beta(\gamma_n - \gamma_\beta)) + \tanh(\beta\gamma_\beta)}{\tanh(\beta(1 - \gamma_\beta)) + \tanh(\beta\gamma_\beta)} \quad (15)$$

where  $\beta$  represents the projection slope,  $\gamma_\beta$  represents the projection point, and  $\gamma_p$  represents the new design variable after the hyperbolic tangent projection.

### 2.3. Optimization Objective Functions

This article optimizes the comprehensive performance of the liquid cooling plate from both thermal and flow performance perspectives. In terms of thermal performance, the focus was on minimizing the average temperature of the battery during high-rate discharge as well as achieving temperature uniformity. These two aspects are represented by minimizing the dimensionless average temperature (Objective 1) and minimizing the dimensionless temperature gradient (Objective 2), respectively. In addition, minimizing the pressure drop between the inlet and outlet (Objective 3) is attempted to achieve better flow performance. The three objective functions are, respectively, expressed as follows:

$$\begin{aligned}\phi_1 &= \frac{\int T^* d\tau_q}{\int d\tau_q}, \quad \phi_2 = \frac{\int \text{Grad}T^* d\tau_q}{\int d\tau_q}, \quad \phi_3 = p_{\text{in}}^* - p_{\text{out}}^* \\ \text{Grad}T^* &= \sqrt{(\text{Grad}T_x^*)^2 + (\text{Grad}T_y^*)^2}, \quad p_{\text{in}}^* = \frac{\int p^* d\Gamma_{\text{in}}}{\int d\Gamma_{\text{in}}}, \quad p_{\text{out}}^* = \frac{\int p^* d\Gamma_{\text{out}}}{\int d\Gamma_{\text{out}}}\end{aligned}\quad (16)$$

Due to the significant differences in the value ranges of the three objective functions, a normalization coefficient is used to normalize each of the three objective functions separately:

$$\phi_1^N = \frac{\phi_1}{\phi_1^0}, \quad \phi_2^N = \frac{\phi_2}{\phi_2^0}, \quad \phi_3^N = \frac{\phi_3}{\phi_3^0} \quad (17)$$

where  $\phi_1^0$ ,  $\phi_2^0$ , and  $\phi_3^0$  are the normalization coefficients of the three objective functions.

The weighting coefficients are used to combine the three objective functions into a total objective function:

$$\phi = w_1 \cdot \phi_1^N + w_2 \cdot \phi_2^N + (1 - w_1 - w_2) \cdot \phi_3^N \quad (18)$$

According to the research by Zhong et al. [12], the weights are set as  $w_1 = 0.7$ ,  $w_2 = 0.1$ .

In order to obtain meaningful results, a limitation on the fluid volume fraction is imposed on the design domain:

$$\int_{\Omega} \gamma d\Omega \leq V_f \cdot V_{\Omega} \quad (19)$$

where  $V_{\Omega}$  represents the volume of the design domain and  $V_f$  represents the maximum allowable volume fraction of the fluid domain.

After such processing, based on the actual application scenarios of battery thermal management and the desired performance improvements, this article transforms the optimization problem of this structure into a mathematical problem as follows:

$$\left\{ \begin{array}{l} \text{Find } \gamma = (\gamma_1, \gamma_2, \dots, \gamma_i), \gamma_i \in [0, 1] \\ \text{Min } \phi = w_1 \cdot \phi_1^N + w_2 \cdot \phi_2^N + (1 - w_1 - w_2) \cdot \phi_3^N \\ \text{Subject to Eqs. (11)–(15)} \\ \int_{\Omega} \gamma d\Omega \leq V_f \cdot V_{\Omega} \end{array} \right. \quad (20)$$

### 2.4. Geometric Model and Boundary Conditions

The design area and corresponding boundary conditions for two-dimensional topology optimization are shown in Figure 2. Based on the actual dimensions of the rectangular lithium-ion battery (173 mm × 85 mm), the design domain for the two-dimensional topology optimization is regarded as 17 L × 8 L. The performance advantages brought about by

the three inlets have been confirmed in previous studies. This article adopts a three-inlet and three-outlet layout for the inlets and outlets, and places particular emphasis on the discussion of the positions of the inlets and outlets.

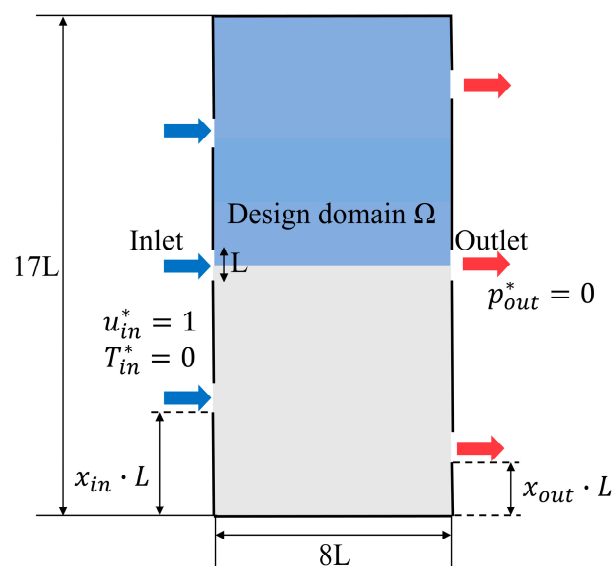


**Figure 2.** Two-dimensional geometric model and boundary conditions for topology optimization.

In order to save computing resources and improve efficiency, this paper only conducts the topology optimization design iteration process for half of the design domain based on the symmetry of the liquid cooling plate and its inlet and outlet arrangements. Based on previous studies [31], comparing the performance of different liquid cooling plates and ensuring that the inlet volumetric flow rate of the liquid is the same is fair. Therefore, for the inlet boundary conditions, this paper sets a constant inlet velocity and inlet temperature. For the outlet boundary conditions, this paper adopts a constant pressure boundary condition, which is consistent with the actual situation. Since this paper only considers the cooling performance of the liquid battery thermal management system, the natural convective heat transfer at the boundaries can be ignored. For the walls other than the inlet and outlet, an insulated boundary condition is set. The important parameters of the topology optimization design problem are shown in Table 1.

**Table 1.** Values of important parameters in the topology optimization design process.

Parameters	Values
Design domain size	17 L × 8 L
Reynolds number Re	150
Darcy number Da	$10^{-4}$
Prandtl number Pr	6.78
The ration of solid and fluid thermal conductivity K	1
Penalty parameter q	0.01
Dimensionless heat transfer coefficient $h^*$	100
Projection slope $\beta$	8
Projection point $\gamma_p$	0.5
Fluid volume fraction $V_f$	0.5

## 2.5. Topology Optimization Solving Procedure

This topology optimization design problem is solved using the multi-physics coupling software COMSOL Multiphysics 6.1. The sequential quadratic programming optimization algorithm (SNOPT) is employed to update the design variables, aiming to achieve an

efficient and precise optimization process. Subsequently, the control equations are solved using the finite element method, and sensitivity analysis is conducted based on the adjoint method. If the difference between the two adjacent optimization results is less than  $10^{-6}$ , the optimization iteration process is stopped and the results are output; otherwise, the same process is repeated.

In order to save computing time while maintaining the accuracy of the calculation, three objective functions were selected as indicators to conduct the grid independence test. Seven grid systems with the number of grids being 3132, 6800, 17,408, 24,939, 33,820, 42,600, and 48,792 were selected for evaluation. As shown in Figure 3, when the grid number is 33,820, the relative errors of the three objective functions are all less than 0.5%. Therefore, for the subsequent topology optimization, the grid density corresponding to the number of grids of 33,820 is selected.

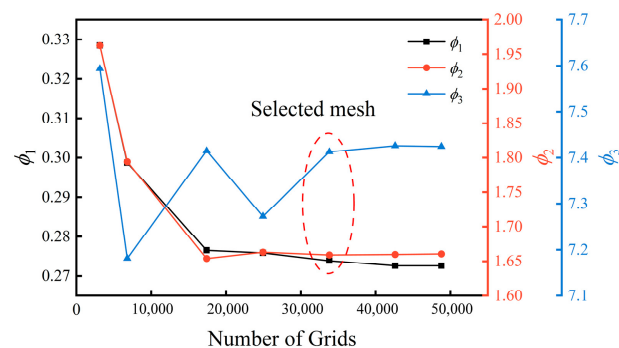


**Figure 3.** Grid independence test in the two-dimensional topology optimization process.

### 3. Three-Dimensional Numerical Simulation Model

#### 3.1. Model Description

A single battery is unable to meet the actual working requirements of an electric vehicle, so multiple batteries are often combined to form a battery pack. As shown in Figure 4a, the battery and the liquid cooling plate are alternately combined to form a battery pack. Aluminum plates of 1 mm thickness are used on both the top and bottom of the flow channel to separate the coolant from the battery. Based on the actual size of the battery (173 mm  $\times$  85 mm), cold plates are expanded in the length and width directions accordingly to prevent coolant leakage. The battery pack is symmetrical in the height direction. To save computing resources, the battery and half of the liquid cooling plates on both sides of it are selected as the simplified research objects, as shown in Figure 4b. The relevant size data are presented in Table 2.

**Table 2.** Physical dimensions of the battery thermal management system.

Parameter	Value (mm)	Parameter	Value (mm)
$L$	173	$H_2$	5
$W$	85	$H_3$	2.5
$E_1$	28	$H_4$	1.5
$E_2$	15	$H_5$	1
$E_3$	7	$b_1$	2.5
$H_1$	21	$b_2$	1.5

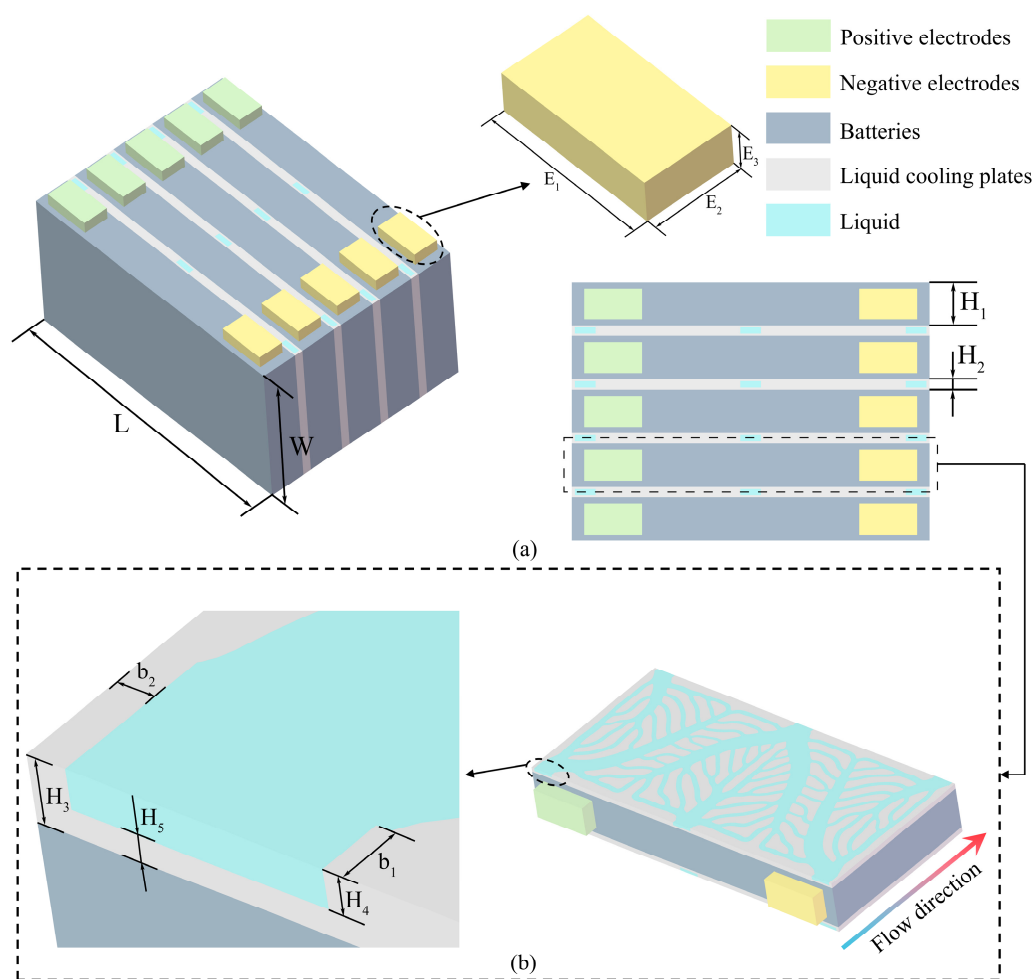


**Figure 4.** (a) Battery pack geometric model and dimensions. (b) Simplified model and dimensions.

### 3.2. Governing Equations for 3D Simulations

During the process of three-dimensional numerical simulation, some assumptions need to be made: the coolant is continuous and incompressible, and the physical parameters of lithium-ion batteries, coolant, and aluminum liquid cooling plates do not change with temperature. The continuity, momentum, and energy equations for the coolant are as follows:

$$\nabla \cdot u_f = 0 \quad (21)$$

$$\rho_f \left( \frac{\partial u_f}{\partial t} + u_f \cdot \nabla u_f \right) = -\nabla P_f + \mu_f \nabla^2 u_f \quad (22)$$

$$\rho_f C_{p,f} \left( \frac{\partial T_f}{\partial t} + u_f \cdot \nabla T_f \right) = \nabla \cdot (k_f \nabla T_f) \quad (23)$$

where  $u_f$ ,  $P_f$ , and  $T_f$ , respectively, represent the speed, pressure, and temperature of the coolant.  $\rho_f$ ,  $\mu_f$ ,  $C_{p,f}$ , and  $k_f$ , respectively, represent the density, viscosity, specific heat capacity, and thermal conductivity of the coolant. The energy equation of lithium-ion batteries is as follows:

$$\rho_b C_{p,b} \frac{\partial T_b}{\partial t} = \nabla \cdot (k_b \nabla T_b) + Q_b \quad (24)$$

where  $\rho_b$ ,  $C_{p,b}$ ,  $T_b$ , and  $k_b$ , respectively, represent the density, specific heat capacity, temperature, and thermal conductivity of the battery. According to the heat generation model established by Bernardi [32], the heat  $Q_b$  generated by the battery is as follows:

$$Q_b = -IT_b \frac{dE_{oc}}{dT_b} + I(E_{oc} - E) \quad (25)$$

where  $I$ ,  $dE_{oc}/dT_b$ ,  $E_{oc}$ , and  $E$ , respectively, represent the working current of the battery, the entropy coefficient related to density, charging status and temperature, the open-circuit voltage of the battery, and the working voltage of the battery. This study uses a second-order RC equivalent circuit model to establish the relationship of voltage changes during the battery discharge process. The relevant parameters in this model are obtained by fitting during the battery discharge experiment. After obtaining the relationship of voltage changes during the discharge process, it is substituted into the formula of the heat generation model to obtain the heat generation. The values of the physical parameters of the battery were measured through experiments. The values of the physical parameters of each material in the battery thermal management system are shown in Table 3.

**Table 3.** Physical parameters of the battery thermal management system.

Material	$\rho$ ( $\text{kg}\cdot\text{m}^{-3}$ )	$C_p$ ( $\text{J}\cdot\text{kg}^{-1}\cdot\text{K}^{-1}$ )	$k$ ( $\text{W}\cdot\text{m}^{-1}\cdot\text{K}^{-1}$ )	$\mu$ ( $\text{Pa}\cdot\text{s}$ )
Solid/aluminum	2719	871	202.4	
Fluid/water	998.2	4182	0.6	0.001003
Positive tab	2719	871	202.4	
Negative tab	8978	381	387.6	
Battery	1986.2	853.6	19.61 (x), 19.61 (y), 7.78 (z)	

### 3.3. Boundary Conditions for Three-Dimensional Numerical Simulation

Set the constant inlet flow rate and inlet temperature boundary conditions as follows:

$$u = u_{in}, T = T_{in} \quad (26)$$

Set the constant pressure outlet boundary condition as follows:

$$P = P_{out} \quad (27)$$

Considering the natural convective heat transfer between the outer surface of the liquid battery thermal management system and the external environment,

$$Q_e = h_{ext} \cdot A_{out} (T_{bout} - T_{ext}) \quad (28)$$

The simplified model is derived based on the symmetry of the battery pack. Therefore, symmetric boundary conditions need to be applied to the upper surface of the upper half of the liquid cooling plate and the lower surface of the lower half of the liquid cooling plate. Apply the no-slip condition at all the contact surfaces between fluids and solids. The capacity of this individual lithium-ion battery is 22.25 Ah. To investigate the battery's heat dissipation under high-rate discharge conditions, a discharge rate of 5C was adopted. This numerical simulation process was carried out in Ansys Fluent. Convergence requires that the residual of the continuity equation be less than  $10^{-4}$ , the residual of the momentum equation be less than  $10^{-6}$ , and the residual of the energy equation be lower than  $10^{-6}$ . The specific values related to the boundary conditions are shown in Table 4.

**Table 4.** Specific parameters of boundary conditions.

Parameters	Values	Unit
Inlet temperature $T_{\text{in}}$	298.15	K
Natural convective heat transfer coefficient with respect to the external environment $h_{\text{ext}}$	5	$\text{W} \cdot \text{m}^{-2} \cdot \text{K}^{-1}$
External temperature $T_{\text{ext}}$	298.15	K
Outlet pressure $P_{\text{out}}$	0	atm
Inlet velocity $u_{\text{in}}$	0.03	$\text{m} \cdot \text{s}^{-1}$

### 3.4. Parameter Definitions

During the operation of the battery, the maximum temperature  $T_{\max}$  and the average temperature  $T_{\text{avg}}$  of the battery can serve as indicators to reflect the cooling performance of the thermal management system of the liquid battery. The average temperature of the battery is defined as follows:

$$T_{\text{avg}} = \frac{\int_{V_b} T dV_b}{\int_{V_b} dV_b} \quad (29)$$

In addition, the ability of the liquid cooling plate to balance the temperature uniformity of the battery can be reflected by the standard deviation of the battery temperature  $T_{\sigma}$ :

$$T_{\sigma} = \sqrt{\frac{\int_{V_b} (T - T_{\text{avg}})^2 dV_b}{\int_{V_b} dV_b}} \quad (30)$$

The total heat removed by the coolant can be defined as follows:

$$Q_f = m_f C_{p,f} (T_{f,\text{out}} - T_{f,\text{in}}) \quad (31)$$

where  $m_f$ ,  $C_{p,f}$ ,  $T_{f,\text{out}}$ , and  $T_{f,\text{in}}$  are, respectively, defined as the inlet mass flow rate of the coolant, the specific heat capacity of the coolant, the average temperature of the coolant at the outlet, and the average temperature of the coolant at the inlet. The average heat transfer coefficient of a fluid  $h_{\text{avg}}$  is defined as follows:

$$h_{\text{avg}} = \frac{Q_f}{A_{\text{sur}} \Delta T_{s,f}} \quad (32)$$

$$\Delta T_{s,f} = T_{\text{sur,avg}} - T_{f,\text{avg}} \quad (33)$$

$$T_{f,\text{avg}} = \frac{T_{f,\text{in}} + T_{f,\text{out}}}{2} \quad (34)$$

where  $A_{\text{sur}}$ ,  $T_{\text{sur,avg}}$ , and  $T_{f,\text{avg}}$ , respectively, represent the contact area between the coolant and the liquid cooling plate, the average temperature of the contact surface between the coolant and the liquid cooling plate, and the average temperature of the coolant at the inlet and outlet.

The average Nusselt number  $Nu$  is defined as follows:

$$Nu = \frac{h_{\text{avg}} \cdot D_h}{k_f} \quad (35)$$

where  $D_h$  represents the hydraulic diameter, which can be defined as follows:

$$D_h = \frac{2 \cdot w \cdot h}{w + h} \quad (36)$$

where  $h$  and  $w$  represent the height and width of the channel.

The pumping power  $P_w$  is an important indicator reflecting the flow performance of the liquid cooling plate structure. Its definition is as follows:

$$P_w = \Delta P_{\text{avg}} \cdot A_{\text{in}} \cdot u_{\text{in}} \quad (37)$$

where  $\Delta P_{\text{avg}}$ ,  $A_{\text{in}}$ , and  $u_{\text{in}}$  represent the pressure drop from the outlet to the inlet, the inlet area, and the inlet flow velocity, respectively.

### 3.5. Verification of Grid Independence

Nusselt number and pressure drop were selected as the reference indicators for the grid independence test. The results of six grid numbers were compared: 1,679,121, 1,980,731, 2,197,103, 2,472,807, 2,725,435, and 3,125,763. When  $x_{\text{in}} = 0$  and  $x_{\text{out}} = 0$ , the numerical simulation was conducted using the boundary conditions described in Table 4, and the results are shown in Figure 5a. For grid systems with a higher density than the one with 2,472,807 elements, the deviation of the two indicators remained below 0.2%. In order to strike a balance between calculation time and calculation accuracy, the grid system with a total of 2,472,807 elements was finally selected for the subsequent three-dimensional numerical simulation, the mesh details of which are also shown in Figure 5a. It can be seen that the grid density is higher at the solid-liquid interface, which is conducive to achieving a balance between accuracy and computation time.

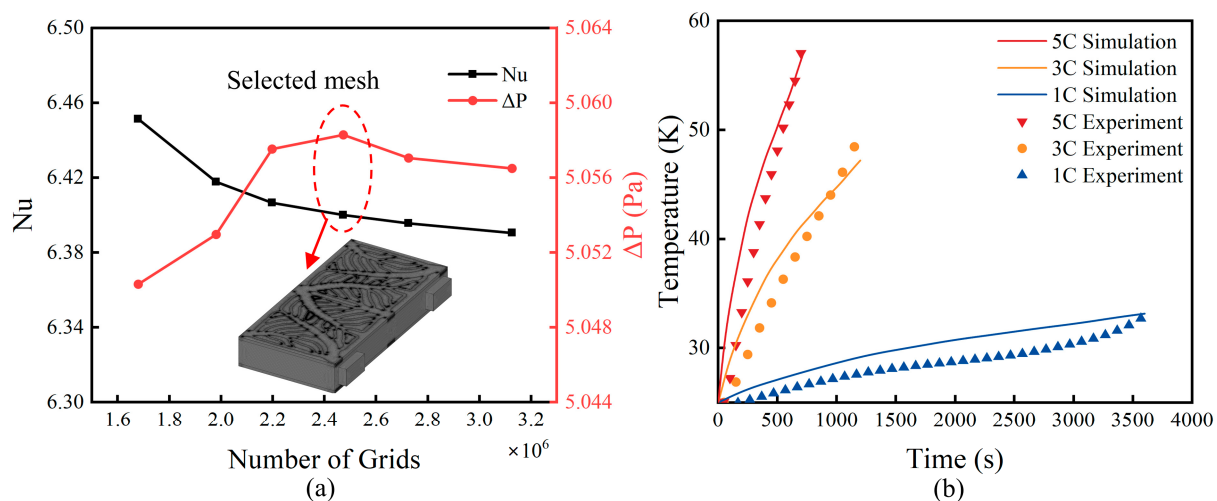


**Figure 5.** (a) Grid independence test for three-dimensional numerical simulation and (b) comparison with experimental data.

This paper conducted battery temperature rise tests under different discharge rates (1C, 3C, 5C) at an environmental temperature of 298.15 K. In the experiment, some thermocouples were used to measure the average temperature on the surface of the battery. These measurements were compared with the numerical simulation data under the corresponding conditions. The relevant data is shown in Figure 5b. It is obvious that the temperature changes obtained from numerical simulations and experiments under different discharge rates show good consistency. This further demonstrates the reliability and validity of the numerical simulation data.

## 4. Results and Discussion

Based on the situation of three inlets and outlets, this study focused on exploring the influence of the positions of the inlets and outlets on the performance of the liquid cooling plate. The values of variables  $x_{\text{in}}$  and  $x_{\text{out}}$  range from 0 to 7. In this study, the considered

range is from 0 to 6. According to actual requirements, the highest temperature at the final discharge moment, the standard deviation of temperature, and the pressure drop are selected as evaluation indicators.

#### 4.1. Single Factor Analysis

Set  $x_{out} = 0$ , and change the values of  $x_{in}$  from 0 to 6 with an interval of 1. The results of the two-dimensional topology optimization conducted at each inlet and outlet position are shown in Figure 6. As the value of  $x_{in}$  increases, the inlets on both sides move towards the center, and the main passage directly connecting the two inlets also shifts towards the center. At the same time, the main passageways that are directly connected to the two sides' outlets have become more prominent, and they gradually extend to both sides. This is due to the need to maintain the uniformity of the overall temperature and the heat exchange performance.

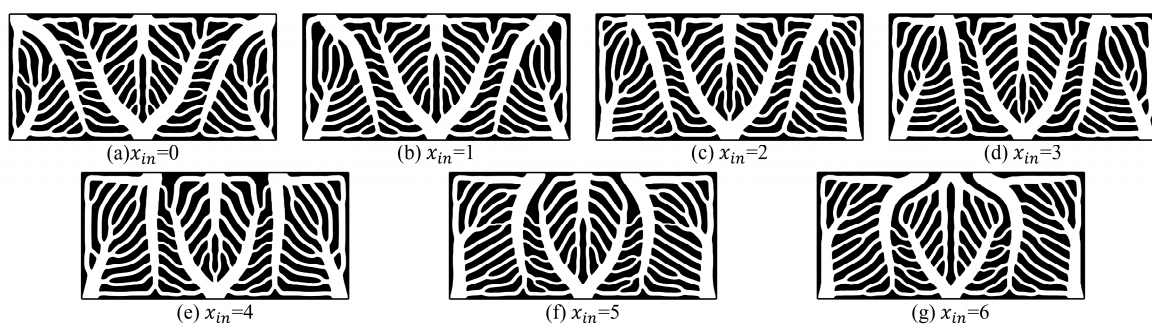


**Figure 6.** Two-dimensional topology optimization results for different inlet positions.

The three evaluation indicators obtained after conducting three-dimensional numerical simulations on the topology optimization results at different inlet positions are shown in Figure 7. It can be seen that all three indicators have become better within the range of  $x_{in}$  from 0 to 2. The maximum temperature shows a fluctuating trend as it increases from 2 to 6. The standard deviation of temperature has been increasing continuously as the value of  $x_{in}$  ranges from 2 to 6, and the situation has become even worse. The pressure drop decreases first and then increases as  $x_{in}$  rises from 2 to 6. The hot spot of the battery is prone to appear in the central area and the edge areas on both sides. As  $x_{in}$  increases from 0 to 6, the main channels at both sides of the inlet gradually change from inward to outward. What this process brings about is a certain change in the concentrated flow area. When  $x_{in} = 2$ , the main channels at both sides of the inlet slightly tilt inward. This allows the flow passing through the middle side of the outlet to increase appropriately while the flow to both sides is not too little, thereby better suppressing the generation of the hot spot, and  $T_{max}$  reaches the lowest point. When  $x_{in}$  is further increased, the main channels at both sides of the inlet deviate outward, so the flow allocated to the middle area of the outlet is insufficient, and  $T_{max}$  increases. The change in  $T_{\sigma}$  is more directly related to the uniform distribution of the flow. When  $x_{in} = 2$ , that is, when the two inlets are, respectively, located in the middle of the outlet and the adjacent side outlet but appropriately deviated to both sides,  $T_{\sigma}$  reaches the lowest value. The size of  $\Delta P$  is related to the bias of the main channel directly connected to the inlet and the length of the flow path. When  $x_{in} = 2\text{--}4$ , the flow paths of the coolant are not too long, so they are at a relatively low level. Since the coolant flows vertically into the flow channel and when the main channels directly connected to both inlet sides are parallel to the coolant's inlet flow direction ( $x_{in} = 4$ ), the impact flow dissipation between the coolant and the solid structure constituting the main channel is the least. Therefore, in this case, the pressure drop is the lowest.

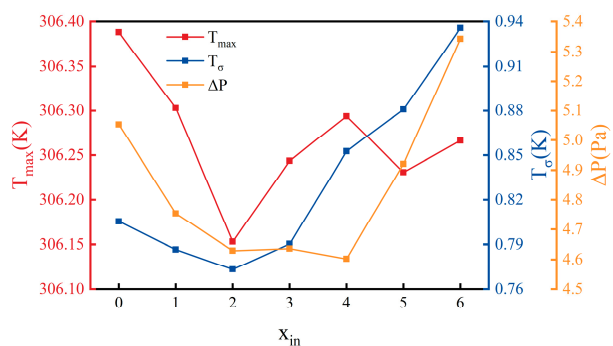


**Figure 7.** Evaluation indicators under different inlet positions.

Set  $x_{in} = 0$ . Then change the value of  $x_{out}$  from 0 to 6, with an interval of 1. The results of the two-dimensional topology optimization at each inlet and outlet position are shown in Figure 8. As  $x_{out}$  increases, the outlets on both sides move towards the center, and the main channel directly connected by the outlets on both sides also moves towards the center. At the same time, the main channel directly connected by the outlets on both sides becomes wider, and the main channel directly connected by the middle outlet gradually disappears.

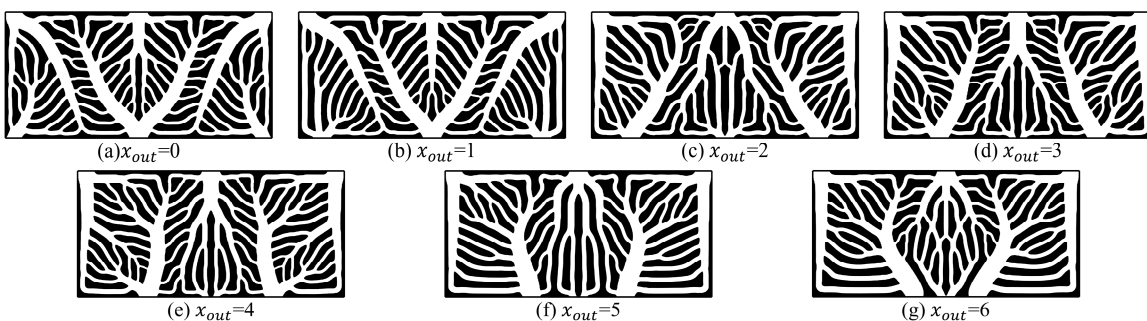


**Figure 8.** Two-dimensional topology optimization results for different outlet positions.

The three evaluation indicators obtained after conducting three-dimensional numerical simulations on the topology optimization results at different outlet positions are shown in Figure 9. It is obvious that the trends of the maximum temperature and the standard deviation of temperature are basically the same, both increasing first, then decreasing, and then increasing again. The reason for the increase in these two indicators first is that the outlet position moves inward, and the coolant entering from both sides flows out from the two outlet sides rapidly. This leads to an inappropriate distribution of flow and a weak effect in suppressing the high-temperature point in the middle of the outlet side. The reason for the subsequent increase and decrease in these two indicators can also be explained by the rationality of the flow distribution. When the outlet positions are located at the middle of the inlets on both sides and slightly closer to the middle ( $x_{out} = 4$ ), the flow distribution is conducive to the uniformity of the battery temperature and the reasonable suppression of the high-temperature point. The pressure drop shows a trend of first decreasing and then increasing, reaching its lowest value when  $x_{out}$  equals 2. This is related to the previously mentioned flow path length. Since the inlets on both sides are located at the edge, a reasonable outlet position on both sides is beneficial to reducing the flow dissipation during the flow process. In addition, the maximum temperature or the standard deviation of temperature is inversely related to the pressure drop. When  $x_{out}$  equals 2, the pressure drop reaches its optimal value, while the maximum temperature and the standard deviation of temperature reach their worst values.

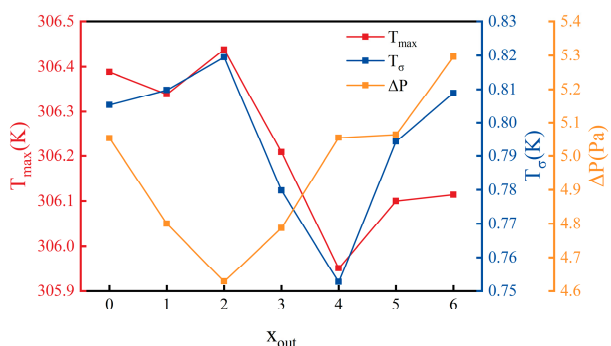


**Figure 9.** Evaluation indicators under different outlet positions.

#### 4.2. Multi-Objective Optimization of Inlet and Outlet Locations

The single-factor analysis based on the control variable method in the previous section can to some extent reflect the relationship between the design factors and the objectives. However, based on the above analysis, it can be found that there are conflicts and complex relationships among the three objectives. By changing the position of the inlet and outlet, there is a complex relationship between reducing the maximum temperature of the battery, reducing the standard deviation of the battery temperature, and reducing the pressure drop of the liquid cooling plate. Due to the complex relationship between the design variables and the responses (evaluation indicators), a strategy is needed to achieve the global optimum. To obtain the optimal design parameters of the inlet and outlet position for topology optimization, this study obtained the set of Pareto front solutions based on the response surface method (RSM) and the non-dominated sorting genetic algorithm II (NSGA-II). Then, the optimal solution was selected from this solution set. As shown in Figure 10a, there is a nonlinear relationship between the position parameters of the inlet and outlet and the three evaluation indicators. This study used orthogonal experimental design to determine the experimental scheme. This way, more information can be obtained with fewer experimental trials. According to the previous section, the optimal values of the three evaluation indicators all fall within the range of 1–5, so the experimental design focuses on capturing the information within this range. Table 5 shows the design parameter levels used for the experimental design.

Subsequently, the response surface method was applied to the three evaluation indicators based on the designed scheme. The fitting degree of the evaluation indicators to the two input factors was evaluated through analysis of variance (ANOVA) [33], and the relevant results are shown in Table 6. The results show that for  $T_{max}$  and  $T_{\sigma}$ , the quadratic model demonstrates excellent statistical significance, while for  $\Delta P$ , the modified cubic model exhibits excellent statistical significance. The P-values of the three fitting models are all less than 0.0001, which proves this point. The  $R^2$  values of the three fitting models are all very close to 1, indicating that the models have excellent predictive performance within the designed experimental scope. The difference between the adjusted  $R^2$  and the predicted  $R^2$  is all less than 0.1, indicating a strong correlation between the observed results and the predicted results. Adequate precision indicates the signal-to-noise ratio, and this value is much greater than 4, indicating that the model has sufficient stability [34]. Figure 10b compares the relationship between the actual evaluation indicators and the predicted evaluation indicators. It can be observed that the predicted values are in close agreement with the actual values, presenting a linear trend with a slope close to 1. This indicates that the established model can accurately and reliably predict the evaluation indicators, which is consistent with the results of the ANOVA analysis. As mentioned above,

these three models can be used to establish the relationship between design variables and evaluation indicators, and the relevant expressions are as shown in Equations (38)–(40).

$$T_{\max} = 306.37669 - 0.239557 \cdot x_{in} - 0.054061 \cdot x_{out} + 0.069240 \cdot x_{in} \cdot x_{out} + 0.039378 \cdot x_{in}^2 - 0.005192 \cdot x_{out}^2 \quad (38)$$

$$T_{\sigma} = 0.867483 - 0.073874 \cdot x_{in} - 0.029033 \cdot x_{out} + 0.020088 \cdot x_{in} \cdot x_{out} + 0.013796 \cdot x_{in}^2 + 0.001551 \cdot x_{out}^2 \quad (39)$$

$$\Delta P = 5.37165 - 0.449289 \cdot x_{in} - 0.628297 \cdot x_{out} + 0.159161 \cdot x_{in} \cdot x_{out} + 0.066027 \cdot x_{in}^2 + 0.10066 \cdot x_{out}^2 - 0.015678 \cdot x_{in}^2 \cdot x_{out} - 0.010184 \cdot x_{in} \cdot x_{out}^2 \quad (40)$$

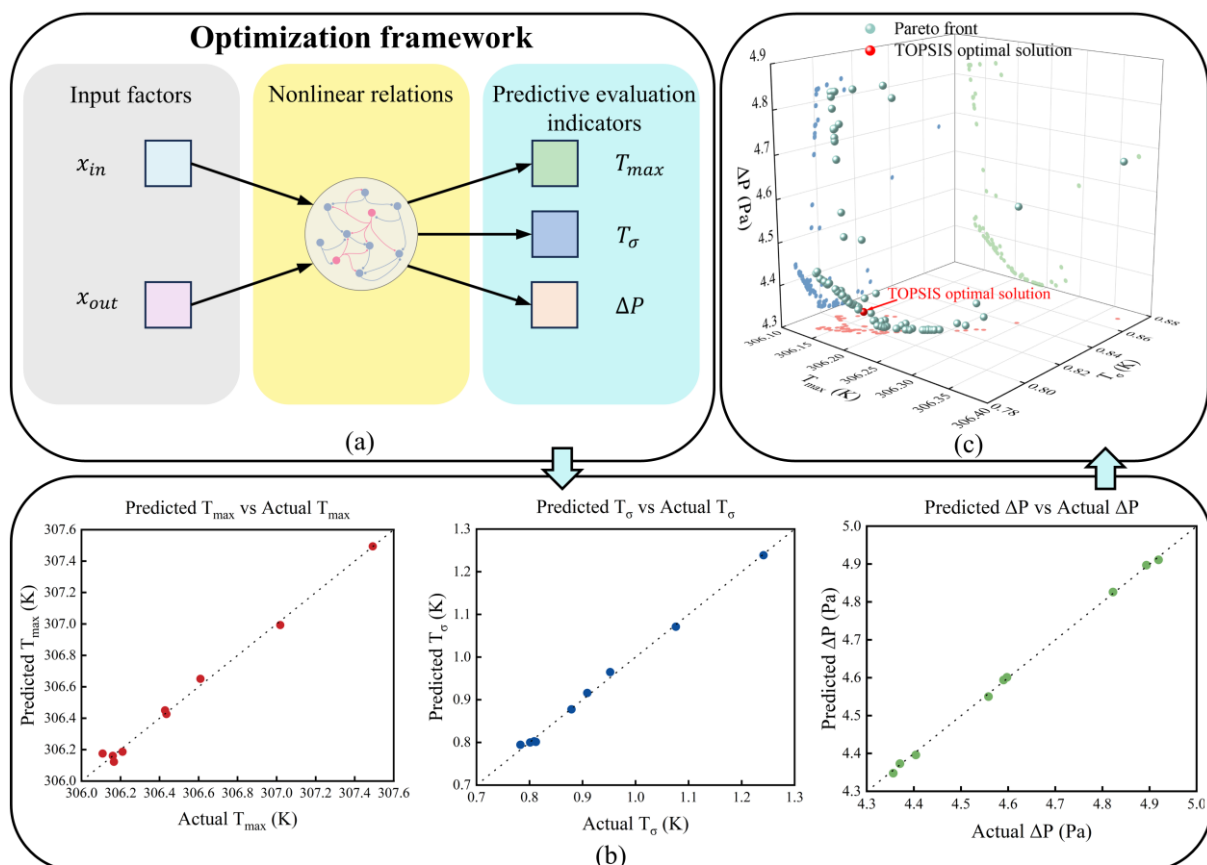


**Figure 10.** (a) Prediction framework between input factors and evaluation indicators; (b) the relationship between the predicted values and the actual values of the evaluation indicators; (c) the values of the evaluation indicators corresponding to the Pareto frontier and the optimal solution obtained using the TOPSIS decision-making strategy.

**Table 5.** Description of the level of design parameters.

Design Parameter	Coded Levels		
	1	2	3
$x_{in}$	1	3	5
$x_{out}$	1	3	5

**Table 6.** ANOVA analysis for three response targets.

Responses	$T_{\max}$	$T_{\sigma}$	$\Delta P$
Order	Quadratic	Quadratic	Modified cubic
$R^2$	0.9942	0.9972	0.9994
P-value	<0.0001	<0.0001	<0.0001
Adjusted $R^2$	0.9901	0.9952	0.9985
Predicted $R^2$	0.9460	0.9726	0.9258
Adequate precision	52.9757	74.6236	85.5677

Therefore, the optimal selection of the input port position can be obtained based on the fitted model derived from RMS. This multi-objective optimization problem is shown in Equation (41), aiming to reduce the maximum temperature of the battery, decrease the standard deviation of the battery temperature, and lower the pressure drop of the liquid cooling plate.

$$\begin{cases} \text{Find } x_{\text{in}}, x_{\text{out}} \\ \text{Minimize } T_{\max} = y_1(x_{\text{in}}, x_{\text{out}}) \\ \text{Minimize } T_{\sigma} = y_2(x_{\text{in}}, x_{\text{out}}) \\ \text{Minimize } \Delta P = y_3(x_{\text{in}}, x_{\text{out}}) \\ x_{\text{in}} \in [1, 5], x_{\text{out}} \in [1, 5] \end{cases} \quad (41)$$

Based on the content of the previous section, it can be observed that there is a complex interplay of gains and losses among the three evaluation indicators in the optimization process. Use NSGA-II to obtain the Pareto front of the optimal solution. NSGA-II has been successfully applied to the optimization of battery thermal management systems. It features the elite non-dominated sorting method and significantly reduces the computational requirements through an efficient sorting algorithm. The important parameters set by NSGA-II are shown in Table 7. Figure 10c presents the Pareto front obtained by the NSGA-II algorithm. The figure shows the three evaluation indicators corresponding to each inlet/outlet position parameter under the solution. An appropriate decision-making scheme is of vital importance for identifying the optimal solution from the Pareto frontier solution set. This study employs TOPSIS to select the optimal solution from the Pareto frontier solution set. This method is based on ideal points and non-ideal points for calculation. To achieve the screening purpose, make the distance between the optimal solution and the non-ideal points the greatest, and the distance between the optimal solution and the ideal point the smallest:

$$d_{i+} = \sqrt{\sum_{j=1}^m (F_{ij} - F_j^{\text{ideal}})^2} \quad (42)$$

$$d_{i-} = \sqrt{\sum_{j=1}^m (F_{ij} - F_j^{\text{non-ideal}})^2} \quad (43)$$

$$i_{\text{final}} = i \in \max \left( \frac{d_{i-}}{d_{i+} + d_{i-}} \right) \quad (44)$$

where  $m$  represents the number of evaluation indicators,  $F_{ij}$  denotes the  $j$ -th evaluation indicator of the  $i$ -th Pareto front solution set,  $F_j^{\text{ideal}}$  is the ideal point of the  $j$ -th evaluation indicator, and  $F_j^{\text{non-ideal}}$  is the non-ideal point of the  $j$ -th evaluation indicator. The final optimal solution obtained is  $x_{\text{in}} = 2.132$ ,  $x_{\text{out}} = 1.552$ . In order to verify the accuracy of the model's predictions, a numerical model was developed for the topology optimization results under the given inlet and outlet parameters. Table 8 presents a comparison between the predicted results and the actual numerical simulation results. The results show

that the error of the predicted values for all evaluation indicators is within 2%, indicating the reliability of the established prediction model and the reliability of the optimal solution obtained.

**Table 7.** Important parameter settings of NSGA-II.

Parameter	Value
Population size	100
Maximum number of iterations	2000
Mutation probability	0.1
Crossover probability	0.9

**Table 8.** Comparison between the predicted value and the simulated value of the optimal solution.

Evaluation Indicator	Predicted Value	Simulated Value	Error
$T_{\max}$ (K)	306.177641	306.0944013	0.027%
$T_{\sigma}$ (K)	0.797838244	0.812113659	1.758%
$\Delta P$ (Pa)	4.344973923	4.318736201	0.608%

#### 4.3. Performance Comparison of Liquid Cooling Plates with Different Structures

This section aims to verify the advantages of the topology-optimized liquid cooling plate structure after optimizing the inlet and outlet layout, and to reveal the reasons for its enhancement. As shown in Figure 11, the thermal management performance of batteries with four channel structures was compared under high-rate discharge (5C): the topology-optimized liquid cooling plate with the optimal inlet and outlet arrangement (TOPO), the topology-optimized liquid cooling plate with the conventional inlet and outlet arrangement (TOPC), the straight channel liquid cooling plate with the optimal inlet and outlet arrangement (SPO), and the single-inlet and single-outlet straight channel liquid cooling plate (SSSP). In addition, this section also discusses the influence of the inlet flow velocity on the thermal management performance of the battery.

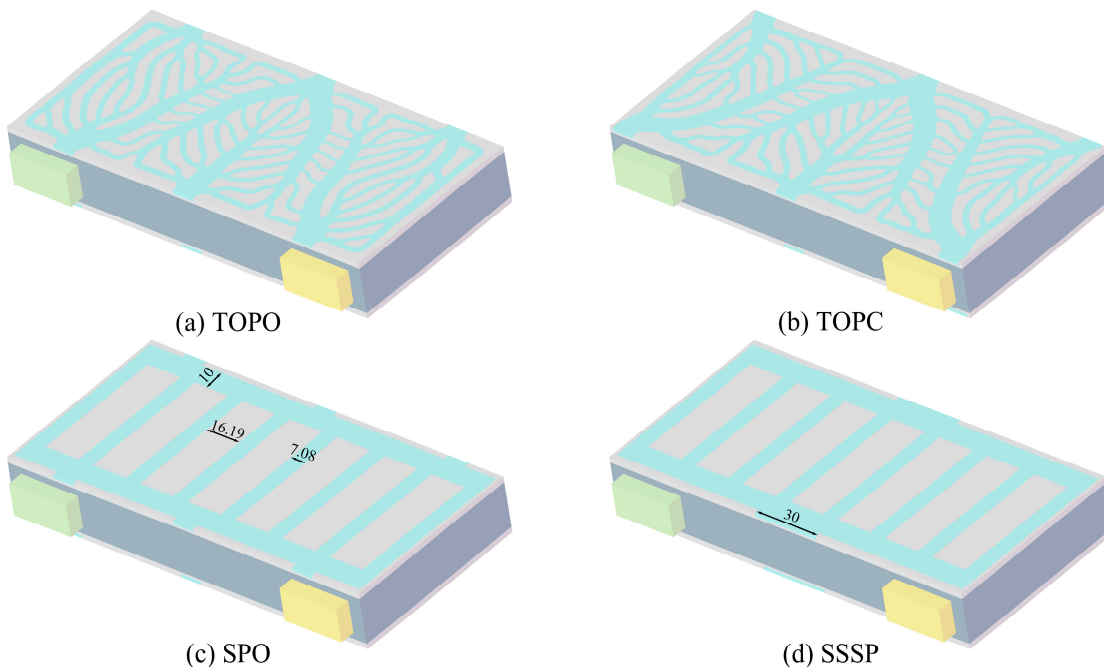


**Figure 11.** Different liquid cooling plate models and size specifications.

For the thermal management system of liquid batteries, it is crucial to simultaneously enhance both thermal performance and flow performance. Therefore, in addition to the evaluation indicators mentioned earlier, define the performance evaluation criterion (PEC) as a comprehensive indicator for evaluating the heat dissipation performance and flow performance. It is a commonly used indicator for assessing the overall performance of the liquid cooling plate. The calculation method of PEC is as follows [24]:

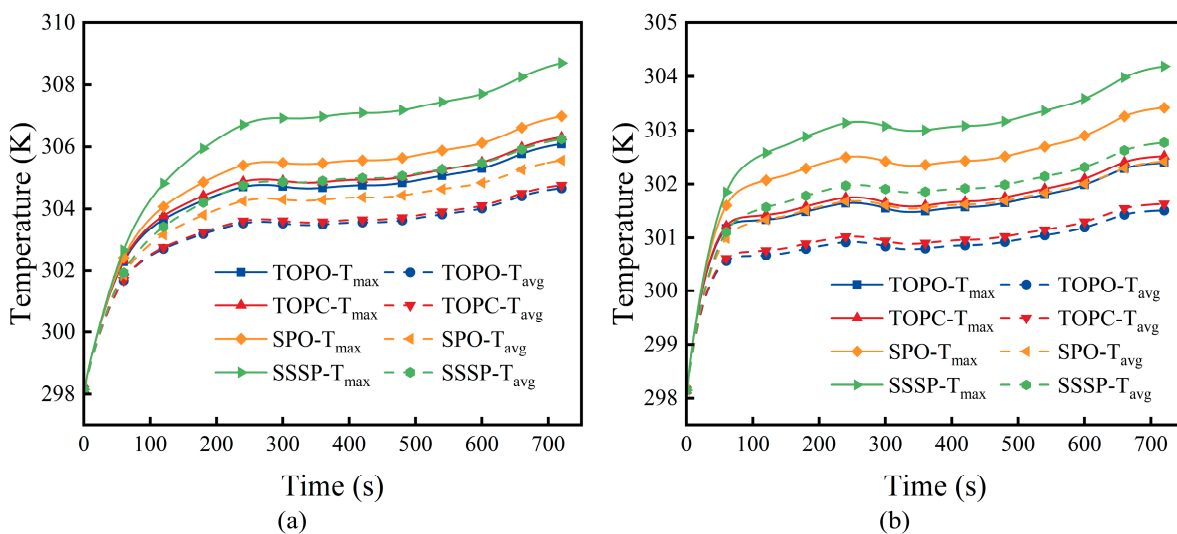
$$PEC = \frac{Nu/Nu_{SSSP}}{(\Delta P/\Delta P_{SSSP})^{\frac{1}{3}}} \quad (45)$$

where  $Nu_{SSSP}$  and  $\Delta P_{SSSP}$  represent the Nusselt number of SSSP and the pressure drop of SSSP, respectively.

Figure 12 shows the changes over time of the maximum and average temperatures of the battery during its operation (with the boundary conditions as described in Table 4), when the battery is cooled by using four different liquid cooling plates. This study presents corresponding images for representative lower inlet velocities (0.03 m/s) and higher velocities (0.13 m/s). All the curves exhibited the same trend: they rose rapidly at first, then fluctuated slowly upwards and reached the peak temperature at the final moment of discharge. It is obvious that after optimizing the layout of the inlets and outlets,  $T_{avg}$  and  $T_{max}$  of TOPO during operation are both lower than those of TOPC with the regular layout of inlets and outlets. Compared with the two straight current channels (SPO, SSSP), TOPO demonstrated a more significant advantage in terms of  $T_{avg}$  and  $T_{max}$  throughout the entire operation process. Among them, SPO, due to the use of optimized inlet and outlet layout, shows a significant trend in terms of  $T_{avg}$  and  $T_{max}$  compared to SSSP. In addition, at high inlet velocities, the advantage of using the TOPO in reducing temperature is more obvious. For example, in Figure 12a, the  $T_{max}$  of TOPO is higher than the  $T_{avg}$  of SPO, but in Figure 12b, the  $T_{max}$  of TOPO is lower than the  $T_{avg}$  of SPO. Based on this figure, the following conclusions can be drawn: 1. Compared with the conventional inlet and outlet layout, the topology-optimized liquid cooling plate, after optimizing the inlet and outlet layout, has to some extent reduced the average temperature and the maximum temperature of the battery during its entire operation process. 2. The optimized inlet and outlet layout applied to the straight channel results in a significant reduction in the average and maximum battery temperatures compared to the traditional single inlet and single outlet configuration. 3. At high inlet velocities, the advantage of temperature relief brought by the topology-optimized liquid cooling plate is more obvious compared to other liquid cooling plates.

Figure 13 shows the variations in the maximum temperature ( $T_{max}$ ), average temperature ( $T_{avg}$ ), temperature standard deviation ( $T_\sigma$ ), and Nusselt number ( $Nu$ ) of the battery with respect to the inlet flow velocity. As the inlet flow rate increases, the  $T_{max}$ ,  $T_{avg}$ , and  $T_\sigma$  of the batteries using the four liquid cooling plates all show a downward trend, while the Nusselt number shows an upward trend. In addition, as the inlet flow rate increases, the extent of these indicators' changes gradually decreases. For different inlet flow rates, the superiority or inferiority of the performance indicators generally follows the following relationship: TOPO > TOPC > SPO > SSSP. Interestingly, as the inlet flow rate increases, TOPO shows a trend of further expanding its advantages compared to SPO, which only has a different flow channel structure. Compared with an inlet flow velocity of 0.03 m/s, when the inlet flow velocity is 0.13 m/s, the  $T_{max}$  and  $T_{avg}$  of TOPO decrease by 3.7 K and 3.16 K, respectively, while the  $T_{max}$  and  $T_{avg}$  of SPO decrease by 3.57 K and 3.15 K, respectively. This trend is more pronounced in terms of the uniformity of battery temperature. Compared with an inlet flow velocity of 0.03 m/s, when the inlet flow velocity is 0.13 m/s, the  $T_\sigma$  of TOPO decreases by 35%, while the  $T_\sigma$  of SPO decreases by 28%. Compared with

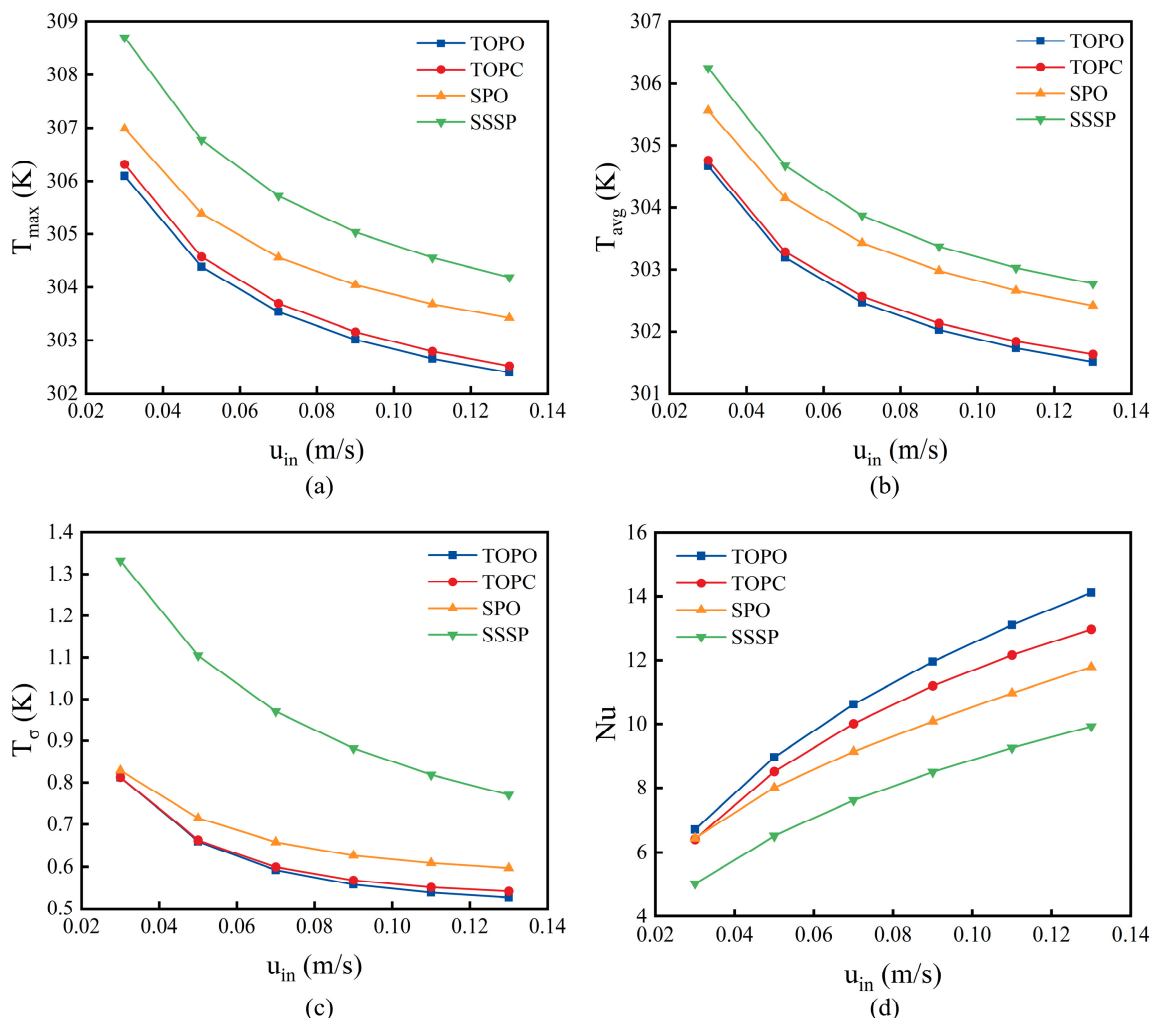
an inlet flow velocity of 0.03 m/s, when the inlet flow velocity was 0.13 m/s, the  $Nu$  of TOPO increased by 7.42 and that of SPO increased by 5.36. Under different inlet flow rates, compared with the other three liquid cooling plate structures, TOPO's  $Nu$  increases by 4.6–8.8%, 4.1–19.7%, and 33.3–42.2%, respectively. It is obvious that as the inlet flow rate increases, TOPO shows a trend of gradually expanding its advantages over SPO in various indicators. This demonstrates that the topology-optimized structure has a greater adaptability to different inlet flow rates in terms of thermal performance indicators. In addition, the topology-optimized liquid cooling plates have more fine and numerous branch flow channels and a larger heat exchange area ( $A_{\text{sur},\text{TOPO}} = 0.0250 \text{ m}^2$ ,  $A_{\text{sur},\text{TOPC}} = 0.0249 \text{ m}^2$ ,  $A_{\text{sur},\text{SPO}} = 0.0185 \text{ m}^2$ ,  $A_{\text{sur},\text{SSSP}} = 0.0185 \text{ m}^2$ ), which is also the key reason for its superior performance compared to the straight current channels.



**Figure 12.** Comparisons of  $T_{\max}$ ,  $T_{\text{avg}}$  for different liquid cooling plates for (a)  $u_{\text{in}} = 0.03 \text{ m/s}$ , (b)  $u_{\text{in}} = 0.13 \text{ m/s}$ .

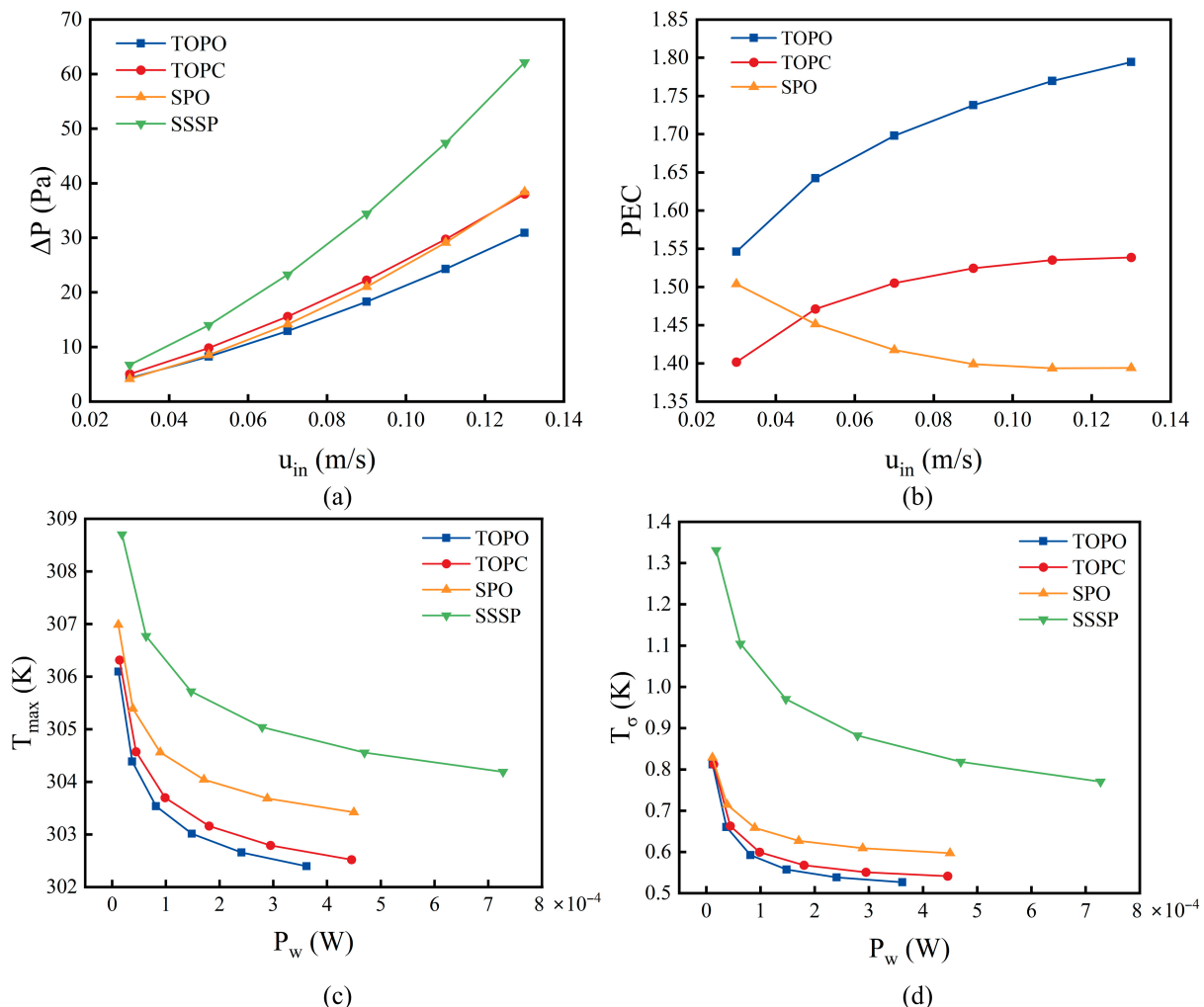
Figure 14a,b show the changes in pressure drop ( $\Delta P$ ) and performance evaluation criterion (PEC) with the variation in inlet flow velocity. For Figure 14a, as the inlet flow velocity increases, the pressure drop of all four liquid cooling plates shows an upward trend. Clearly, as the inlet flow velocity increases, the pressure drop of TOPO is further superior to that of SPO and TOPC. When the inlet flow velocity is 0.03 m/s, the pressure drops of TOPO, TOPC, and SPO are 4.32 Pa, 5.06 Pa, and 4.16 Pa, respectively. At this time, the pressure drop of TOPO is slightly higher than that of SPO because the topology optimization generates more complex channels and has a longer flow path. Therefore, during the flow process, more resistance is received, resulting in a higher pressure drop. When the inlet flow velocity is 0.13 m/s, the pressure drops of TOPO, TOPC, and SPO are 30.92 Pa, 38.06 Pa, and 38.44 Pa, respectively. At this time, the pressure drop of TOPO is significantly lower than that of TOPC and SPO. This indicates that the flow channels generated by topology optimization have a greater advantage at high inlet flow velocities. In addition, the optimized inlet and outlet arrangement can have better thermal performance at different inlet flow velocities while having lower pressure drop. For Figure 14b, as the inlet flow velocity increases, the PEC of TOPO and TOPC both increase, while the PEC of SPO decreases. This further indicates that the topology-optimized channel structure has stronger adaptability to high flow velocities, which is not possessed by traditional straight channels. In addition, as the inlet flow velocity increases, the increase rate of TOPO's PEC is faster, and the comprehensive performance advantage of TOPO compared to other flow channel structures is further expanded. Compared with the inlet

flow velocity of 0.03 m/s, when the inlet flow velocity is 0.13 m/s, the PEC of TOPO increases by 0.24, and the PEC of TOPC increases by 0.14. The increase rate of TOPO's PEC is 1.7 times that of TOPC, and the comprehensive performance advantage brought by the optimized inlet and outlet arrangement is considerable.



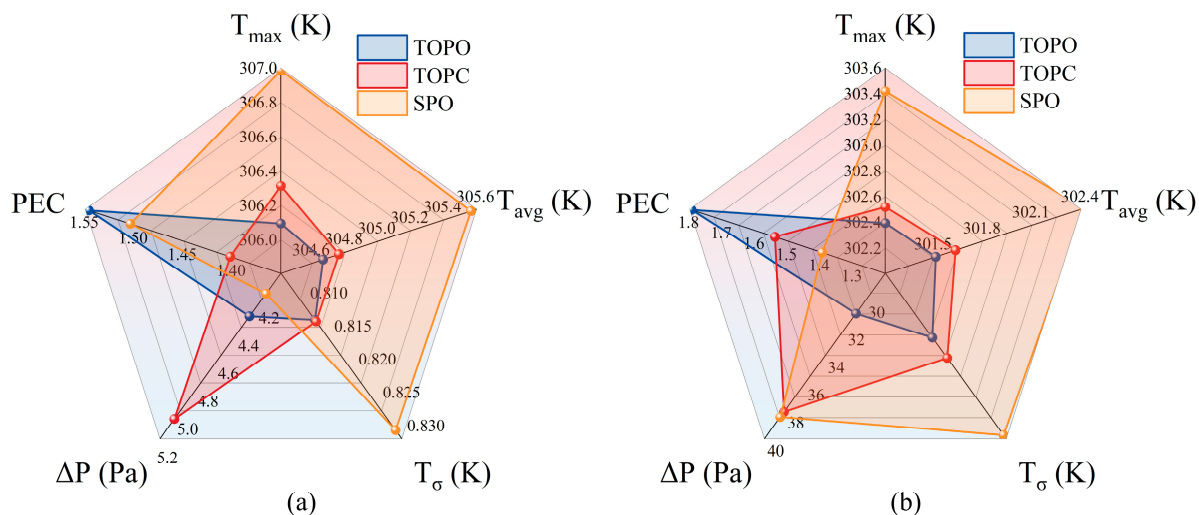
**Figure 13.** Under different inlet flow rates, the variations in the four liquid cooling plates in (a) the maximum temperature, (b) the average temperature, (c) the temperature standard deviation, and (d) the Nusselt number.

Figure 14c,d show the variations in the maximum temperature ( $T_{max}$ ) and the standard deviation of the temperature ( $T_\sigma$ ) under four different liquid cooling plates at different pumping powers. It is obvious that although the increase in pumping power is becoming increasingly significant, the improvements in the maximum battery temperature and the standard deviation of temperature are becoming smaller and smaller. Therefore, choosing the appropriate pumping power (that is, achieving a balance between pumping power and performance improvement) is of crucial importance in practical applications. For the four liquid cooling plate structures studied in this paper, TOPO can achieve better heat dissipation performance and temperature uniformity under the same pumping power, which is helpful in solving the energy issues in practical applications.



**Figure 14.** Under different inlet flow rates (or pumping powers), the variations in the four liquid cooling plates in (a) the pressure drop, (b) performance evaluation criterion, (c) maximum temperature, and (d) temperature standard deviation.

Figure 15 shows the various indicators of the three liquid cooling plates (TOPO, TOPC, SPO) under the conditions of inlet flow velocities of 0.03 m/s and 0.13 m/s. Except for PEC, where larger is better, all the other indicators are better when smaller. It is obvious that when the inlet flow rate is 0.03 m/s, TOPO is not the best among the three liquid cooling plates in terms of some indicators such as pressure drop. However, when the inlet flow rate was 0.13 m/s, TOPO achieved the best results in all five indicators and had a much greater advantage gap. Table 9 presents in greater detail the five evaluation indicators corresponding to the four liquid cooling plates when the inlet flow velocity is 0.03 m/s and 0.13 m/s. First, a comparison between TOPO and TOPC is conducted to analyze the effect of optimizing the layout of inlets and outlets. Within the range of inlet flow velocity from 0.03 to 0.13 m/s, compared with TOPC, TOPO's  $T_{max}$  decreased by 0.13–0.22 K,  $T_{avg}$  decreased by 0.096–0.121 K,  $T_\sigma$  decreased by 0.03–2.72%, pressure drop decreased by 14.62–18.75%, and PEC increased by 10.3–16.61%. Then there is a comparison with the traditional straight channels that are currently widely used. Within the range of inlet flow velocity from 0.03 to 0.13 m/s, compared with the two straight channels (SPO, SSSP), the  $T_{max}$  of TOPO decreased by 0.9–2.6 K, the  $T_{avg}$  decreased by 0.9–1.6 K, the  $T_\sigma$  decreased by 2–40%, the pressure drop decreased by –3.93–50.25%, and the PEC increased by 2.82–79.43%.



**Figure 15.** The comparison of various indicators when the inlet flow velocity is (a) 0.03 m/s and (b) 0.13 m/s.

**Table 9.** The various evaluation indicators of the four liquid cooling plates under low inlet flow rate (0.03 m/s) and high inlet flow rate (0.13 m/s).

Evaluation Indicators	$u_{in}$ (m/s)	TOPO	TOPC	SPO	SSSP
$T_{\max}$ (K)	0.03	306.094	306.314	306.986	308.702
$T_{\max}$ (K)	0.13	302.394	302.519	303.420	304.189
$T_{\text{avg}}$ (K)	0.03	304.667	304.763	305.566	306.251
$T_{\text{avg}}$ (K)	0.13	301.511	301.631	302.420	302.771
$T_{\sigma}$ (K)	0.03	0.812	0.812	0.829	1.331
$T_{\sigma}$ (K)	0.13	0.527	0.542	0.597	0.770
$\Delta P$ (Pa)	0.03	4.319	5.058	4.156	6.742
$\Delta P$ (Pa)	0.13	30.921	38.058	38.435	62.156
PEC	0.03	1.546	1.402	1.504	1.000
PEC	0.13	1.794	1.539	1.394	1.000

Figure 16 shows the velocity distribution and flow lines within the flow channels of the four liquid cooling plates when the inlet flow velocity is 0.13 m/s. All four liquid cooling plates have a relatively high flow velocity at the inlet and outlet, but the two topology-optimized flow channels (TOPO, TOPC) have a more uniform velocity distribution. Since the layout of TOPO is more uniform, its uniformity of velocity distribution is better than that of TOPC. In contrast, both the straight channels have uneven flow distribution, and the coolant flows rapidly from the proximal straight channel to the outlet. SSSP, due to its single inlet, exhibits this phenomenon more significantly. This is the main reason for the poor cooling performance of the two straight channels, as the coolant does not adequately stay in the channels for heat exchange. The flow line analysis further explains the reasons for the differences in flow performance. Compared to the obvious vortices near the inlet of TOPC, the inlets on both sides of TOPO eliminate this phenomenon. This is because one of the objectives of optimizing the inlet and outlet layout is pressure drop, and reducing unnecessary vortices to lower the pressure drop is one of the objectives. And because the inlet coolant temperature is low, it can effectively carry away the heat generated by the adjacent battery at the inlet. Therefore, the flow recirculation area near the inlet is unnecessary and is not conducive to the overall heat dissipation performance. In contrast, SPO and SSSP have very large ranges of vortices. However, the vortex distribution of SPO is more uniform, and the positions for enhancing local heat transfer are more uniform. This

is one of the reasons why the thermal performance such as battery temperature uniformity is better with SPO than SSSP. The biomimetic structure similar to the root of a tree obtained through topology optimization design is conducive to making the coolant distribute more smoothly and uniformly in the flow channels. Such a flow channel structure can largely reduce flow loss and correspond to its advantages in flow performance.

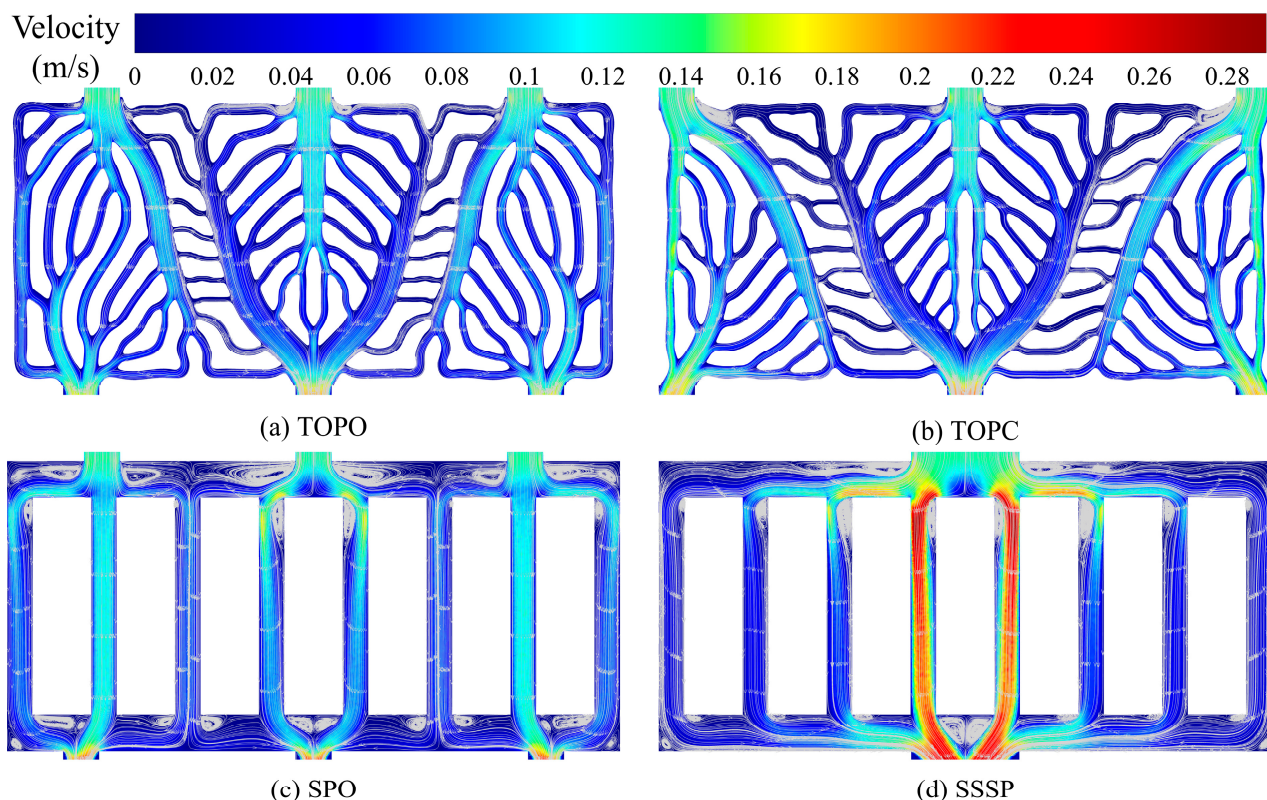


**Figure 16.** Velocity distributions and streamlines within flow channels of the four liquid cooling plate configurations when the inlet velocity is 0.13 m/s.

Figure 17 shows the temperature distribution diagrams of the battery discharge at the final moment when the inlet flow velocity is 0.13 m/s, under the application of four types of liquid cooling plates. The four figures show similar temperature distribution patterns. The battery temperature near the inlet is very low. This is because the coolant temperature at the inlet is low and the flow rate is high, which can effectively remove the heat from the battery. As the coolant moves away from the inlet, it continuously absorbs the heat from the battery, causing the temperature to gradually increase and the cooling effect to gradually weaken. Compared with the two straight channels (SPO, SSSP), the battery temperatures of the two topology optimization channel structures (TOPO, TOPC) are significantly lower, and the heat dissipation effect is better. According to Figure 16, TOPO has a more uniform velocity distribution. Compared with TOPC, TOPO has a more uniform temperature distribution and a wider cooling effect in the flow direction. Since the middle area and the two side areas on the outlet side are the areas where high-temperature points are likely to occur. The flow distribution of TOPO achieves a balance where the highest temperature in these areas with high-temperature points is the lowest. This explains why the high-temperature area at the outlet surface under TOPO is smaller and the maximum temperature is lower.

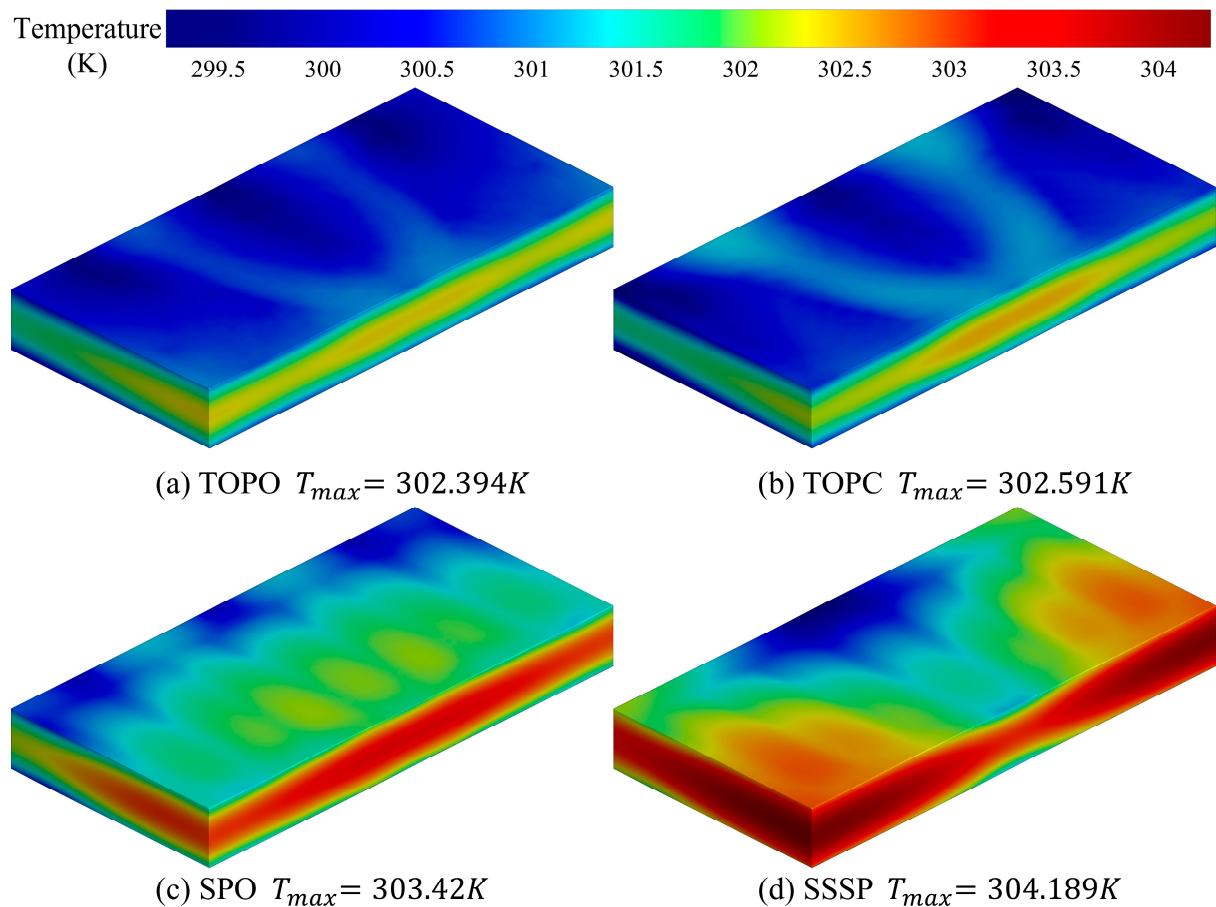


**Figure 17.** Temperature distributions for four liquid cooling plates when the inlet velocity is 0.13 m/s.

## 5. Conclusions

This study employed the topology optimization method to obtain the optimal liquid cooling plate structure for the liquid battery thermal management system (BTMS). Based on the situation of three inlets and three outlets in the width direction, a comprehensive discussion was conducted on the parameters of the inlet and outlet positions. The relationship between the design parameters (distances of side inlets/outlets from the edges) and the evaluation indicators (maximum battery temperature  $T_{max}$ , temperature standard deviation  $T_\sigma$ , and pressure drop  $\Delta P$ ) was established using the response surface method (RSM). Subsequently, the Pareto front was obtained using the Non-dominated Sorting Genetic Algorithm II (NSGA-II), and the optimal solution was obtained using the TOPSIS strategy. Finally, a comprehensive comparison of the thermal management performance and flow performance was conducted between the topology-optimized liquid cooling plate with the optimal inlet and outlet arrangement (TOPO), the topology-optimized liquid cooling plate with the conventional inlet and outlet arrangement (TOPC), the straight channel liquid cooling plate with the optimal inlet and outlet arrangement (SPO), and the single-inlet and single-outlet straight channel liquid cooling plate (SSSP). The main conclusions are as follows:

1. When the outlet positions are fixed on both sides and the inlet positions are changed, the trends of the three evaluation indicators are relatively similar. When the inlet positions are fixed on both sides and the outlet positions are changed, the three evaluation indicators show a significant alternation phenomenon. In general, it is difficult to simultaneously achieve the optimization of all three indicators.

2. The expression of the design variables and the three evaluation indicators ( $T_{\max}$ ,  $T_{\sigma}$ ,  $\Delta P$ ) was constructed using the response surface method, with  $R^2$  values of 0.9942, 0.9972, and 0.9994, respectively. According to the NSGA-II and TOPSIS decision methods, the optimal solution was  $x_{\text{in}} = 2.132$ ,  $x_{\text{out}} = 1.552$ . The numerical verification indicates that the maximum relative error does not exceed 2%.

3. The BTMS using TOPO achieved better evaluation indicators ( $T_{\max}$ ,  $T_{\text{avg}}$ ,  $T_{\sigma}$ ,  $\Delta P$ , and performance evaluation criterion PEC) than using TOPC under different inlet flow rates. Among them, the advantage of PEC under different inlet flow rates was 10.3–16.61%.

4. TOPO has a more significant performance advantage for the other liquid cooling plates at high inlet flow rates (0.13 m/s) compared to low inlet flow rates (0.03 m/s).

5. At high inlet flow rates (0.13 m/s), compared with the traditional straight channel liquid cooling plate (SPO, SSSP), TOPO improved PEC by 28.7% and 79.4%, respectively.

The results of this study indicate that the liquid cooling plate structure obtained through topology optimization can improve the heat transfer efficiency while reducing the required power consumption simultaneously. In addition, by optimizing the positions of the inlets and outlets, the heat transfer efficiency can be further enhanced under a reduced power consumption. However, the flow channel structures obtained through topology optimization seem to be complex, which may impose challenge on the manufacturability and mass production. It is worth noting that with the rapid development of additive manufacturing technology, techniques such as selective laser melting provide promising solutions for mass production of cold plates. In addition, the mesh density of the topology optimization design can be limited to the accuracy required by traditional processing methods, in which way the liquid cooling plate structure obtained through topology optimization could meet the manufacturing accuracy requirements of large-scale production machine tools.

**Author Contributions:** T.Y.: writing—original draft, visualization, validation, methodology, investigation, formal analysis, data curation; H.L.: writing—review & editing, writing—original draft, supervision, resources, project administration, funding acquisition, conceptualization; W.Z.: writing—review & editing, validation, investigation, data curation; A.D.: writing—review & editing, project administration, funding acquisition; M.W.: writing—review & editing, project administration, funding acquisition. All authors have read and agreed to the published version of the manuscript.

**Funding:** This research was financially supported by National Key Research and Development Program of China (Grant No. 2023YFB4301703), National Natural Science Foundation of China (Grant No. 52306070), the Dalian High Level Talent Innovation Support Program (2024RQ009), Innovation Team Project of the Chinese Ministry of Education of China (8091B042204), Key Research and Development Program of Jiangxi Province (Grant No. 20244BBG73009), and the Fundamental Research Funds for the Central Universities (Grant No. 3132025124).

**Data Availability Statement:** The data presented in this study are available on request from the corresponding author. The data are not publicly available due to privacy.

**Conflicts of Interest:** Author Aoshuang Ding was employed by the company CSSC Jiujiang Boiler Co., Ltd; Author Mengke Wu was employed by the company Locomotive Development Department, CRRC Dalian Locomotive and Rolling Stock Co., Ltd.. The remaining authors declare that the research was conducted in the absence of any commercial or financial relationships that could be construed as a potential conflict of interest.

## References

1. Liu, D.; Xu, L.; Sadia, U.H.; Wang, H. Evaluating the CO<sub>2</sub> emission reduction effect of China's battery electric vehicle promotion efforts. *Atmos. Pollut. Res.* **2021**, *12*, 101115. [CrossRef]
2. Ji, H.; Luo, T.; Dai, L.; He, Z.; Wang, Q. Topology design of cold plates for pouch battery thermal management considering heat distribution characteristics. *Appl. Therm. Eng.* **2023**, *224*, 119940. [CrossRef]

3. Zhang, X.; Li, Z.; Luo, L.; Fan, Y.; Du, Z. A review on thermal management of lithium-ion batteries for electric vehicles. *Energy* **2022**, *238*, 121652. [[CrossRef](#)]
4. Jouhara, H.; Khordehgah, N.; Serey, N.; Almahmoud, S.; Lester, S.P.; Machen, D.; Wrobel, L. Applications and thermal management of rechargeable batteries for industrial applications. *Energy* **2019**, *170*, 849–861. [[CrossRef](#)]
5. Liu, H.; Wei, Z.; He, W.; Zhao, J. Thermal issues about Li-ion batteries and recent progress in battery thermal management systems: A review. *Energy Convers. Manag.* **2017**, *150*, 304–330. [[CrossRef](#)]
6. Zhao, G.; Wang, X.; Negnevitsky, M.; Li, C. An up-to-date review on the design improvement and optimization of the liquid-cooling battery thermal management system for electric vehicles. *Appl. Therm. Eng.* **2023**, *219*, 119626. [[CrossRef](#)]
7. Khoshvaght-Aliabadi, M.; Abbaszadeh, A.; Salimi, A.; Salehi, N. Structural modifications of sinusoidal wavy minichannels cold plates applied in liquid cooling of lithium-ion batteries. *J. Energy Storage* **2023**, *57*, 106208. [[CrossRef](#)]
8. Shahjalal, M.; Shams, T.; Islam, M.E.; Alam, W.; Modak, M.; Hossain, S.B.; Ramadesigan, V.; Ahmed, M.R.; Ahmed, H.; Iqbal, A. A review of thermal management for Li-ion batteries: Prospects, challenges, and issues. *J. Energy Storage* **2021**, *39*, 102518. [[CrossRef](#)]
9. Chen, K.; Wu, W.; Yuan, F.; Chen, L.; Wang, S. Cooling efficiency improvement of air-cooled battery thermal management system through designing the flow pattern. *Energy* **2019**, *167*, 781–790. [[CrossRef](#)]
10. Akbarzadeh, M.; Kalogiannis, T.; Jaguemont, J.; Jin, L.; Behi, H.; Karimi, D.; Beheshti, H.; Van Mierlo, J.; Berecibar, M. A comparative study between air cooling and liquid cooling thermal management systems for a high-energy lithium-ion battery module. *Appl. Therm. Eng.* **2021**, *198*, 117503. [[CrossRef](#)]
11. Chen, Z.; Yang, S.; Pan, M.; Xu, J. Experimental investigation on thermal management of lithium-ion battery with roll bond liquid cooling plate. *Appl. Therm. Eng.* **2022**, *206*, 118106. [[CrossRef](#)]
12. Zhong, Q.; Chandra, P.K.; Li, W.; Gao, L.; Garg, A.; Lv, S.; Tai, K. A comprehensive numerical study based on topology optimization for cooling plates thermal design of battery packs. *Appl. Therm. Eng.* **2024**, *236*, 121918. [[CrossRef](#)]
13. Sheng, L.; Zhang, H.; Su, L.; Zhang, Z.; Zhang, H.; Li, K.; Fang, Y.; Ye, W. Effect analysis on thermal profile management of a cylindrical lithium-ion battery utilizing a cellular liquid cooling jacket. *Energy* **2021**, *220*, 119725. [[CrossRef](#)]
14. Zhang, F.; Gou, H.; Xie, C.; He, Y.; Zhu, Y.; Lu, F.; Liang, B.; Xiao, K. A new stepped-channel liquid cooling plate thermal management system combined with composite phase change materials. *Appl. Therm. Eng.* **2022**, *211*, 118439. [[CrossRef](#)]
15. Ge, X.; Li, X.; Jin, Y.; Zhang, G.; Deng, J.; Ge, J. Experimental investigation on thermal management system of composite phase change material coupled with serpentine tubes for battery module. *Appl. Therm. Eng.* **2023**, *219*, 119501. [[CrossRef](#)]
16. Zhao, Y.; Zhang, X.; Yang, B.; Cai, S. A review of battery thermal management systems using liquid cooling and PCM. *J. Energy Storage* **2024**, *76*, 109836. [[CrossRef](#)]
17. Jhariya, M.; Dewangan, A.K.; Moinuddin, S.Q.; Kumar, S.; Ahmad, A.; Yadav, A.K. Research progress on efficient battery thermal management system (BTMs) for electric vehicles using composite phase change materials with liquid cooling and nanoadditives. *J. Therm. Anal. Calorim.* **2024**, *149*, 13653–13680. [[CrossRef](#)]
18. Thakur, A.K.; Sathyamurthy, R.; Velraj, R.; Saidur, R.; Pandey, A.; Ma, Z.; Singh, P.; Hazra, S.K.; Sharshir, S.W.; Prabakaran, R. A state-of-the art review on advancing battery thermal management systems for fast-charging. *Appl. Therm. Eng.* **2023**, *226*, 120303. [[CrossRef](#)]
19. Liu, H.; Gao, X.; Zhao, J.; Yu, M.; Niu, D.; Ji, Y. Liquid-based battery thermal management system performance improvement with intersected serpentine channels. *Renew. Energy* **2022**, *199*, 640–652. [[CrossRef](#)]
20. Fan, Y.; Wang, Z.; Fu, T.; Wu, H. Numerical investigation on lithium-ion battery thermal management utilizing a novel tree-like channel liquid cooling plate exchanger. *Int. J. Heat Mass Transf.* **2022**, *183*, 122143. [[CrossRef](#)]
21. Xia, H.; Wang, J.; Shen, Y.; Fang, K. A liquid-cooled plate based on bionic flow channels evolved from the shape of leaf veins and tree roots. *Int. J. Therm. Sci.* **2025**, *208*, 109468. [[CrossRef](#)]
22. Zhong, Q.; Gao, L.; Li, W.; Zhao, J.; Garg, A.; Panda, B. A novel preheating systems for columnar lithium batteries for below zero degrees celsius environment based on topology optimization. *Int. Commun. Heat Mass Transf.* **2024**, *158*, 107789. [[CrossRef](#)]
23. Zhan, S.; Chen, Y.; Yin, Y.; Li, Z.; Yu, C. Examining the influence of number of inlets and outlets on the topology optimization design of battery liquid cooling plate. *Appl. Therm. Eng.* **2024**, *252*, 123691. [[CrossRef](#)]
24. Wang, Z.; Zou, Z.; Zhou, Y.; Geng, X.; Sun, Y.; Huang, X.; Hao, M. Performance comparison of battery cold plates designed using topology optimization across laminar and turbulent flow regime. *Int. J. Heat Mass Transf.* **2025**, *238*, 126450. [[CrossRef](#)]
25. Zhan, S.; Cheng, Z.; Yin, Y.; Yu, C.; Zhao, C. Effect of inlet and outlet positions on heat dissipation performance of lithium-ion battery cold plates: An analysis based on topology optimization. *Int. J. Heat Mass Transf.* **2023**, *215*, 124436. [[CrossRef](#)]
26. Lin, X.-W.; Shi, M.-Y.; Zhou, Z.-F.; Chen, B.; Lu, Y.-J.; Jing, D.-W. Multi-objective topology optimization design of liquid-based cooling plate for 280 Ah prismatic energy storage battery thermal management. *Energy Convers. Manag.* **2025**, *325*, 119440. [[CrossRef](#)]
27. Wu, J.P.; Liu, H.L.; Li, C.C.; Li, C.H.; Xie, G. Topological optimization and thermal performance of cold plates for lithium-ion battery with non-uniform heat sources. *Appl. Therm. Eng.* **2024**, *254*, 123922. [[CrossRef](#)]

28. Qian, S.; Lou, S.; Ge, C.; Wang, W.; Tian, X.; Cai, Y. The influence of temperature dependent fluid properties on topology optimization of conjugate heat transfer. *Int. J. Therm. Sci.* **2022**, *173*, 107424. [[CrossRef](#)]
29. Wu, Y.; Li, Z.; Zhi, C.; Li, Z.; Shi, C.; Tan, G.; Ming, T. Pseudo three-dimensional topology optimization of cold plates for electric vehicle power packs. *Int. J. Heat Mass Transf.* **2024**, *232*, 125966. [[CrossRef](#)]
30. Zhang, K.; Li, Y.; Chang, S.-M.; Hu, L.; Wang, X.; Yu, M. Hydraulic and thermal performance enhancement for the cold plate using topology optimization. *Appl. Therm. Eng.* **2024**, *236*, 121829. [[CrossRef](#)]
31. Xia, Y.; Chen, L.; Luo, J.; Tao, W. Numerical investigation of microchannel heat sinks with different inlets and outlets based on topology optimization. *Appl. Energy* **2023**, *330*, 120335. [[CrossRef](#)]
32. Wang, J.; Shao, Z.; Du, J.; Chen, F.; Song, Z. Effects of inlet and outlet configurations on the topological optimization design of cooling plates for lithium-ion batteries. *J. Energy Storage* **2024**, *79*, 110124. [[CrossRef](#)]
33. Sui, Z.; Lin, H.; Sun, Q.; Dong, K.; Wu, W. Multi-objective optimization of efficient liquid cooling-based battery thermal management system using hybrid manifold channels. *Appl. Energy* **2024**, *371*, 123766. [[CrossRef](#)]
34. Yan, W.; Meng, X.; Cui, X.; Liu, Y.; Chen, Q.; Jin, L. Evaporative cooling performance prediction and multi-objective optimization for hollow fiber membrane module using response surface methodology. *Appl. Energy* **2022**, *325*, 119855. [[CrossRef](#)]

**Disclaimer/Publisher's Note:** The statements, opinions and data contained in all publications are solely those of the individual author(s) and contributor(s) and not of MDPI and/or the editor(s). MDPI and/or the editor(s) disclaim responsibility for any injury to people or property resulting from any ideas, methods, instructions or products referred to in the content.